South Malvinas/Falkland Basin: hydrocarbon migration and petroleum system.

Martino Foschi (corresponding author)

Shell Geoscience Laboratory – Department of Earth science, University of Oxford, South Parks Road, Oxford, OX1 3AN, UK

martinof@earth.ox.ac.uk

Joseph Albert Cartwright

Shell Geoscience Laboratory – Department of Earth science, University of Oxford, South Parks Road, Oxford, OX1 3AN, UK

joec@earth.ox.ac.uk

Abstract

We report a detailed seismic interpretational study of direct hydrocarbon indicators (DHIs) using 2D multichannel seismic reflection data. The study includes analyses of four distinctive types of DHI: (1) a bottom simulating reflection (BSR), (2) enhanced reflections (ERs), (3) pipes and vertical anomaly clusters, which indicate focused migration of hydrocarbon fluids, and (4) flat spots which indicate a deeper source for the shallower hydrocarbon occurrences. The interpretation of these DHIs included analysis of spatial distribution, amplitude variation with offset (AVO) and instantaneous spectral decomposition. These analyses are set in a tectono–stratigraphic context in order to evaluate the relationship between intra–basinal

structures, hydrocarbon occurrences and migration pathways. The recent discovery of a gas condensate accumulation in the study area (Darwin well, ca.190MMbbl) confirms the presence of a mature source rock in the basin and supports a model whereby the observed DHIs are connected via an active hydrocarbon plumbing system.

1. Introduction

Hydrocarbon plumbing systems (HPSs) are assemblages of permeable pathways that allow hydrocarbons to ascend from the deeper kitchen area of a basin where they are generated to shallower reservoirs where they can become trapped in sufficient quantities to form commercial accumulations (Andresen, 2012). The pathways involved in any given HPS are highly variable, depending on geological context, but generally involve a combination of stratal (along bedding) and cross–stratal hydrocarbon migration (England et al., 1987). One of the most enigmatic aspects of secondary hydrocarbon migration is the common observation that shallow accumulations often occur directly above the kitchen, but are separated by several thousand metres of low permeability sediments (Aplin et al., 1999). This observation led Cartwright et al. (2007) to suggest that highly focused vertical hydrocarbon migration may move mainly through a diverse set of geological features that they termed seal bypass systems, and which can be subdivided into three main classes: (1) faults, (2) intrusions, (3) pipes. Berndt (2005), Imbert (2009), Andresen and Huuse (2011) and Andresen (2012), among others, developed similar ideas to account for the array of observations stemming from multi–attribute 3D seismic interpretation in areas of active vertical fluid and hydrocarbon flow. Andresen (2012) in particular showed how it is possible to group a set of seemingly disparate fluid flow phenomena observed on seismic data, such as a bottom simulating reflection (BSR), pipes, and pockmarks, and link them together explicitly as part of a single connected flow system. Where hydrocarbons are proven to be part of the flow, then this can in turn be described as an HPS.

Subsequently, Anka et al. (2012) and Ostanin et al. (2013) have taken the analysis of HPSs to a more advanced level using a similar approach, but by introducing additional data such as geochemistry of surface hydrocarbon seeps and numerical modelling of source rock maturation and hydrocarbon migration into their analytical framework.

In this paper, we focus on the challenges confronting those interested in analysing HPS in frontier basins, where there may be few or no wells available, no geochemical data, and only 2D, rather than 3D seismic data. We focus on a geophysical approach to augment classical observations of direct hydrocarbon indicators (DHIs). The central aim of this paper is to develop an integrated geophysical interpretation using quantitative techniques such as amplitude versus offset (AVO) and frequency analysis to document either in situ hydrocarbons or features that indicate the passage of hydrocarbons through the sediment column. Then, following the approach developed by Andresen (2012), by collating and analysing the distribution of DHIs and fluid flow features, to examine whether their spatial relationships suggest a causal association such that the assemblage could reasonably be grouped into a HPS. A secondary aim is to discuss the likely origin of hydrocarbons, and discuss whether thermogenenic, biogenic or some mixture of the two best accounts for the observed distributions and the geometry of the HPS.

The study area is the South Malvinas/Falkland Basin (SMFB; Figure 1), a region that has received only limited research attention (e.g. Ludwig, 1983; Platt and Philip, 1995; Bry et al., 2005). Petroleum exploration in this frontier exploration area is also relatively recent, with few wells drilled to date but potential for working petroleum systems to match those identified with drilling further North-East on the Malvinas/Falklands Plateau Basin (Richards et al., 1996; Fish, 2005). The primary geophysical data available to interpret the HPS in this area are 2D reflection seismic, and as such this is an ideal case study area in which to adopt a more quantitative geophysical approach to analysing an HPS.

2. Data and methods

2.1. Seismic and well data

The entire South Malvinas/Falkland Basin (SMFB) has been imaged by a number hydrocarbon exploration and scientific multichannel reflection seismic surveys (Ludwig, 1893; Richards et al., 1996; Platt and Philip, 1995; Fish, 2005). The seismic dataset used in this work is composed of two 2D seismic surveys (Figure 1B) provided by Falkland Oil and Gas Limited (FOGL) and Geophysical Service Incorporated (GSI).

The FOGL dataset was acquired using multiple airguns and streamers with 480 channels and a sampling interval of 2ms. The nominal fold was of 120 traces per common mid–point (CMP) and a trace length of 8s TWT. The survey was processed using a work–flow focused on multiple removal, which included surface related multiple elimination (SRME) and demultiple Radon transform. Full Kirchhoff pre–stack time migration has been applied to restore the position of the reflections in time domain. The GSI dataset acquisition parameters were not provided. The processing applied to the GSI dataset is similar to the one applied to the FOGL dataset. However the GSI processing flow included anisotropic time migration and F–X deconvolution. These differences on the processing flow provided a larger frequency bandwidth of the final migrated dataset and a clearer definition of the seismic image.

Both seismic surveys are composed of two angle–stack and full–stack seismic sections. This allowed computing analysis in pre–stack domain (near and far domain). The FOGL dataset included also velocity stack data in time domain which have been used to perform time-to-depth conversion of some key lines. This process has been performed by using Halliburton-Landmark ProMAX (see Methods).

The combination of surveys gives a variable grid spacing of 2–8 km. The surveys are zero–phase with an SEG standard polarity where positive peaks represent an increase in acoustic

impedance across an interface (Brown, 2004), referred to here as positive reflections. The vertical seismic resolution of the dataset is variable and partly a function of the different processing sequences applied to data from different surveys. However, given the typical frequency content between 30 and 45Hz and a velocity variation between 1600 and 1900m/s the vertical resolution, defined approximately as ¼ of the dominant wavelength (Widess, 1973), ranges between 10 and 12m.

No direct well calibration was possible in this study. Results from several recently drilled wells are not available although some stratigraphic and petroleum data have been released via exploration company websites and are used here with the appropriate caveats, noted below. The Darwin discovery represents the most important indication of the presence of a working petroleum system in the study area. Darwin was drilled in 2012 by Border & Southern PLC and is located just over a kilometre from the closest seismic profile in the available database (Figure 1B). Border & Southern PLC released some information in 2012 (Border & Southern, 2012a and 2012b), in which they confirm Darwin as a gas condensate discovery. Source–prone intervals were encountered at two stratigraphic levels in the well, but were found to be immature for hydrocarbon generation. The mature source rock responsible for the discovery is suggested to be present 320m below the base of the well (Figure 2DD).

2.2. Methods

The 2D seismic data have been interpreted using computer–aided interpretational software (GeoFrame and Petrel) provided by Schlumberger. Time–to–depth conversion of some key 2D profiles was performed by (1)applying interval-to-smoothed velocity data provided by FOGL and (2) using standard time-to-depth conversion module present in Halliburton-Landmark ProMAX. Time, depth, and thickness maps, derived from the interpretation of the 2D seismic grid, have been created by using convergent interpolation algorithms present in Geoframe. For

these operations a limited search windows, set to 1 km, was use to constrain the extent of the maps and maintain a more reliable extrapolation of the values of the picked horizons.

Due to the lack of precise borehole calibration of the seismic data, detailed litho– and chrono–stratigraphic descriptions of the seismic stratigraphy of the basin has not been possible. The interpretation of the stratigraphic units present in the SMFB is therefore based on the previous published work focused in the study area (e.g. Bry et al., 2005; Fish, 2005; Platt and Philip, 1995). A framework of major regionally correlatable seismic horizons (B, B1 and C, Figure 2A) has been used to define two major seismic packages in the study area. These packages are used to analyse the seismic facies of host units and the habitat of the DHIs.

The qualitative interpretation of the seismic amplitude data has been augmented by quantitative analyses of the amplitude variation with offset (AVO). AVO analyses of a range of amplitude anomalies were performed using standard approaches in order to discriminate seismic anomalies associated with lithological variations from anomalies potentially caused by the presence of hydrocarbons (Castagna and Smith, 1994). The results were plotted using the standard intercept versus gradient cross–plot technique (Castagna and Swan, 1997).

3. Geological Setting

The SMFB lies at the southern margin of the South America plate and is located ~200 km south of the Malvinas/Falkland Islands (Figure 1). The structural style of the SMFB, interpreted as a partially-filled foreland basin (Bry et al., 2004; Richards et al., 1996), is broadly similar to that of the adjacent Malvinas Basin (Baristeas et al., 2013; Galeazzi, 1998; Ghiglione et al., 2010; Tassone, 2008). The SMFB is bounded to the East and to the south by a major E-W sinistral mostly-transpressional, and transtensional, transform fault (Esteban et al., 2013) which account for the deformation between the South American plate and the Scotia Plate (Scotia-

South America plate boundary, SSAPB; Figure 1). The SMFB is bounded to the West by the Malvinas Basin and to the North by the Malvinas/Falkland Islands (Figure 1A).

3.1 Tectonic evolution and structural setting

Prior to break-up of Gondwana, the SMFB was located to the SW of the Karoo Basin (Platt and Philip, 1995; Macdonald et al., 2003; Verard et al., 2012). At that time the Malvinas/Falkland Islands were oriented approximately 120 degrees with respect to the present day configuration (Stone et al., 2009). During the Early Jurassic the South American and Antarctic plates started to move to South-West, and easterly direction, respectively (Verard et al., 2012). This early pattern of break-up and plate movement is thought to have been the period of marked clockwise rotation of the Malvinas/Falkland Islands and adjacent basins (Macdonald et al., 2003). The orientation of the SMFB would have changed substantially during this period with rotation ceasing in the Late Jurassic, as discussed by Stone et al., (2009). Rifting and extension of the SMFB, and also the East Malvinas/Falkland Basin, are associated with the continued break-up of Gondwana that started in the Late Jurassic (initial breakup at ~155Ma, Verard et al., 2012). This stage of crustal stretching is expressed on the seismic data by a series of approximately E–W striking normal faults with planar to gently listric geometry, dipping mostly to the North (Figure 2A–B–C).

The early post-rift stage (Early Cretaceous) is accompanied in the South America plate by the opening of the South Atlantic Ocean (Davison, 1999). In the late post-rift phase (Late Cretaceous) a reorganization of the plates generated a widespread unconformity (~70Ma, Macdonald et al., 2003; Late Maastrichtian, Fish, 2005, Zabanbark, 2011) observed in the SMFB (Horizon C, Figure 2) but also in other basins of the Malvinas/Falkland Islands (e.g. Del Ben and Mallardi, 2004). In the early Cenozoic the left-lateral transtensional relative motion of South America and Antartica plates produced the eastward spreading of the

fragmented Pacific margin cordillera which accounted for the formation of the Scotia Ridge (Dalziel et al., 2013).

The continuous motion of the plates facilitated the opening of the Scotia Sea, which commenced at ~40 (Barker, 2001). The continuous thrusting and the increasing in thickness of the Burdwood Bank increased the loading on the rifted basement with a consequent flexural response (Bry et al., 2004; Fish, 2005) and reactivation of the Early Cretaceous normal fault system. This stage, documented by Richards et al (1996) and approximately dated as Late Cretaceous by Fish (2005), is characterised by modest additions (<100 m) of displacement on the normal fault system (Figure 2C). The deformation along the SSAPB accounts for the Neogene wrench deformation within southern Patagonia (Magallanes–Fagnano strike-slip fault zone; Baristeas et al., 2013).

3.2 Seismic stratigraphy

The stratigraphy of the study area can be broadly divided into two main megasequence units based on the gross reflection geometry, the recognition of a major regional unconformity, the termination of major structures and on previously published interpretations (Bry et al., 2005; Fish, 2005; Platt and Philip, 1995).

Unit 1 is interpreted to be Mesozoic in age and corresponds to a combined pre–rift and syn–rift megasequence previously defined by Fish (2005). It has not been possible to separate the pre– and syn–rift throughout the study area, due to the limited occurrence of divergent reflection geometries within the tilted fault blocks. However, locally, abrupt thickness changes across faults can be observed close to the upper limit of this unit, suggesting that most of the displacement occurred towards the end of this megasequence (Figure 2D). Unit 1 can be divided into Sub–units 1a and 1b, on the basis of gross reflection characteristics (Figure 2D).

Sub–unit 1a is composed of very low amplitude laterally continuous reflections partially onlapping the acoustic basement. Sub–unit 1a exhibits southward-thickening with variable thicknesses ranging from 100 to 600m. Sub–unit 1a may include lateral equivalents to the Tobífera Formation as seen in the adjacent Malvinas Basin — calibrated with industry and scientific wells by previous workers (Pucci, 2006; Fish, 2005; Platt and Philip, 1995) — and tentatively assigned as Middle Jurassic to Early Cretaceous in age. Sub–unit 1b is composed of laterally continuous, parallel–stratified reflections that exhibit moderate to high amplitude response. These high amplitude reflections have been correlated to within 14 km of the location of well 61/17–1 and by extrapolation using local dip values in this sub–unit, this package is interpreted to be stratigraphically equivalent to the sandstone reservoir interval encountered in this well (termed the Darwin discovery) (Figure 2A). The high amplitude package intersected by the well and at the depth of the reservoir interval (Figure 2A) also comprises organic rich mudstones. Some of these mudstones may have potential as petroleum source rocks, as suggested in the descriptions of well 61/17–1 (Figure 2DD). Sub–unit 1b thickens slightly to the South across the basin, with values ranging between 700–900m. The upper boundary of Sub–unit 1b is a major unconformity (Horizon C in Figure 2). This boundary is marked by pronounced erosional truncation in the northern area, and a network of valleys/submarine canyons is incised into this surface in the central region of the study area (Figure 2). Based on the well calibration 61/17–1 and published interpretations of the area (Fish, 2005; Platt and Philip, 1995), Sub–unit 1b is approximately dated as Aptian to Late Cretaceous in age.

Unit 2 is identified as a prominent, southward–thickening wedge bounded at its base by Horizon C and at its top by the seabed. Unit 2 corresponds to the post–rift megasequence defined by Fish (2005) (Figure 2D). The geometry of this wedge, clearly observed in Figure 2A, whose maximum thickness is nearly 3km, and the progressive onlap onto Horizon C, are consistent with a flexural subsidence mechanism (Watts and Ryan, 1976) linked to thrust

loading and compressional tectonics related to the tectonic activity along the margins of the Burdwood Bank (Bry et al., 2005). The wedge fill is predominantly composed of divergent, onlapping, laterally continuous reflections that exhibit variable amplitude response from weak to moderate.

Unit 2 is important in the context of the study because it hosts numerous amplitude anomalies (AAs), enhanced reflections (ERs) and a continuous-to-discontinuous seabed simulating negative reflection which was previously observed by Richards et al. (1996) and interpreted as a bottom simulating reflection (BSR, described later). The laterally continuous reflection pattern of Unit 2 is punctuated by several mass transport deposits (MTDs). MTDs are identified as elongate bodies characterised by chaotic reflectivity (c.f. Frey Martinez, 20010; Bull et al. 2009). The MTDs occur mostly in the central region of Unit 2, immediately adjacent to the northern margin of the Burdwood Bank, from which they may be derived. A representative example of MTD is shown in Figure 2A.

In the shallower section of Unit 2 the reflection geometry exhibits an undulating pattern. These sediments exhibit moderate to weak amplitude response and have been previously interpreted by Bry et al. (2005) as contourites. These sediments are composed of mainly silt to fine sands (Cunningham et al., 2002) which have been deposited by the action of water bottom currents (Koenitz et al., 2008). Unit 2 has been inferred to be Cenozoic in age by Bry et al. (2004). A similar interpretation was provided by Richards et al (1996), based on long range calibration with commercial wells located in the adjacent Malvinas Basin.

4. Seismic Interpretation of Direct Hydrocarbon Indicators and Associated Fluid Flow Features

4.1. Bottom Simulating Reflection (BSR)

A discontinuous, negative polarity reflection has been mapped over much of the study area within the uppermost part of Unit 2 (Figure 3). We follow Richards et al. (1996) in interpreting the negative reflection as a BSR because it exhibits all the diagnostic characteristics of BSRs that are universally associated with the base of the Gas Hydrate Stability Zone (BGHSZ). Its polarity, relationships to host stratigraphy and structure, and almost constant depth beneath the seabed are typical of hydrate–related BSRs identified on many other continental margins (e.g. Brooks et al., 1991; Ecker et al., 1998; Helgerud et al., 1999; Korenaga et al., 1997; Satyavani et al., 2003; Shelander et al., 2012).

Polarity and relationship with stratigraphy, structure and seabed surface

The polarity of the BSR is always negative due to the decreasing acoustic impedance with depth produced by gas hydrate–bearing sediments above and the water– or gas–bearing sediments below (Tinivella and Giustiniani, 2013). Five representative traces were extracted from a 2D seismic profile and plotted in Figure 3 to analyse the polarity of the BSR. In trace T1 (Figure 3B) the BSR is a zero–phase negative reflection followed by a number of enhanced reflections beneath. In traces T2, T3, and T4, the BSR exhibits an isolated strong negative amplitude response with amplification approximately 1.5 times higher than the seabed reflection (positive).

The relationship between the BSR and the host stratigraphy is based on the lateral variation in the acoustic response of the BSR throughout the area (Figure 4). In the north of the study area, the BSR is primarily associated with stacked amplitude anomalies in the form of enhanced reflections occurring just beneath the BSR (described later; Figure 4B). These enhanced reflections all exhibit abrupt amplitude reduction to their background values at the BSR, which has a serrate geometry. For example, in Figure 4B and C, the BSR is interpreted as a notional surface or envelope that defines the updip amplitude cut–offs of the enhanced stratal

reflections. This geometry is similar to that of a BSR and its underlying anomalies documented by Calves et al (2009) in the Indus Basin.

In the centre of the basin, the BSR segments are recognised within MTDs (Figure 4DN). The BSR is easily detected because of its different continuous acoustic expression with respect to the chaotic seismic facies of the MTD (Figure 4DN). The region immediately beneath the BSR in the MTD exhibits an amplified chaotic reflection pattern, making it easier to recognise the BSR (Figure 4DN). The BSR is not as easily identifiable in the more stratified, concordant seismic facies, presumably because the BGHSZ is parallel to the strata. In the south, the BSR is easily identified because the stratigraphy is discordant to the seabed, and updip termination or cut–off of steeply dipping enhanced reflections at the BSR envelope is readily interpreted (Figure 4DS).

Based on these interpretational criteria a map showing the extent of the interpreted BSR was constructed (Figure 4A). The interpreted BSR is almost continuous at the northern and southern limits of the area, but in the central zone it is more discontinuous and patchy. The total area covered by the interpreted BSR is 2.53×10^3 km^2.

The relationship between the BSR and the seabed surface was evaluated by comparing time maps of the seabed and the BSR (Figure 5A). The two surfaces have an almost identical geometry over most of the study area, with a general mimicking of the BSR with the seabed as observed widely elsewhere for the BSR (c.f. Calves et al. 2008; Liu and Flemings, 2007) (Figures 4–5). However, in some areas in the northern and eastern regions of the study area, the geometry of the BSR differs from that of the seabed, as can be seen when comparing the contours of the two mapped surfaces which show clear divergent patterns (e.g. crossing contours (CC), Figure 5A). Most strikingly, in the northern region, the BSR shallows from the regional depth value and its shape is convex upwards, with a domal geometry (DSB, Figure 5B).

4.2. Enhanced Reflections (ERs)

The most widely developed class of DHI in the study area is represented by ERs. ERs appear on the seismic data as amplified reflections characterised typically by monotonically decreasing amplitude values with depth (Hustoft et al., 2007). The amplification may be consistent with the geometry of the reflections. In many cases the amplification increases up dip along the ERs and sharply decreases at the BSR (e.g. Fohrmann and Pecher, 2012). ERs developed immediately subjacent to the BSR are typically interpreted as free–gas bearing layers (Holbrook et al., 1996; Wood and Ruppel, 2000; Bünz et al., 2003; Hustoft et al., 2007; Yoo et al., 2013).

The acoustic expression of the ERs is simply that of amplified reflections with respect to their laterally correlative background amplitude values but where the amplification along the reflection decreases with depth (Figure 6A). The individual ERs consist of a prominent highly amplified single negative reflection with constructively interfering side lobe reflections (e.g. Widess, 1973) (Figure 6B). Paired reflections (negative–positive) may potentially define the tops and bases of single lithologically distinctive layers (top and base, Figure 6B). The BSR and the ERs exhibit a strongly serrated or 'roof–tile' configuration similar to that described by Calves et al. (2008) from the Indus Fan (Figure 6C). The acoustic characteristics of the ERs in the study area — namely, their sharp amplitude cut–off at the BSR, negative amplitude response and variations in amplitude with distance and depth — are consistent with many previous descriptions of free gas charged layers beneath the BGHSZ (e.g. Cukur et al., 2013; Hustoft et al., 2007; Li et al., 2013; Sun et al., 2012; Yoo et al., 2013).

The downdip limit of the ERs is qualitatively interpreted as the base of the free gas zone (BFGZ, Figure 6A), and is taken as the point where the amplitude values decrease to the background values. The complicated geometry of the ERs and the variable attenuation below

the BSR partially obscure the interpretation of the BFGZ, but it was nonetheless possible to map the vertical separation in two way travel time from the BFGZ to the BSR (Figure 6D).

The 'time thickness' map of the interpreted free gas zone (Figure 6D) shows the distribution of the substantial accumulations of free gas in two main regions extending approximately east–west with a combined area of 2,200 km^2. These regions are separated by a corridor–like region with only limited accumulations that measures approximately 10–15 km in width. The substantial free–gas regions coincide areally with the normal–fault and the fold–thrust regions.

The potential volume of gas stored within the FGZ has been crudely estimated using sediment property parameters based on sediment core tops obtained 150km to the east of the study area and at depth of 1200–3800m (Cunningham et al., 2002). The seabed sediments are composed of a mixture of silt (measured grain size of 0.004–0.03 mm) and fine sand (measured grain size of 0.125–0.25 mm). The measured silt content is 55% by volume (Cunningham et al., 2002) and the resulting porosity for sediment mixture, assuming a loose random packing (Dullien, 1992), is 0.242 (Koltermann and Gorelick, 1995). Applying a velocity of the sediments of 1.77 km/s from velocity data, an approximate volume of free gas would vary between 1.309×10^9 m^3 (5% gas saturation) and 1.309×10^{10} m^3 (50% gas saturation). The northern zone contains just over 70% of this total, assuming uniformity of porosity and saturation values throughout the area.

4.3. Fluid Expulsion Pipes

Fluid expulsion pipes are not typically referred to as a class of DHI, but they are frequently linked to vertical gas migration (Løseth et al., 2001; Cartwright et al., 2007; Moss and Cartwright, 2010; Andresen and Huuse, 2011). They are therefore included here as a potentially important component of the analysis of a potential HPS (Andresen, 2012). Fluid expulsion

pipes are identifiable on seismic data as a generally columnar zone of vertical disturbance or loss of coherence of the background strata reflections. Fluid expulsion pipes have a range of observed vertical dimensions and aspect ratios (Hustoft et al. 2009; Moss and Cartwright, 2010). Pipes are most frequently described from 3D seismic data, where horizontal slice attributes can be used to constrain the columnar geometry (Hustoft et al. 2009; Moss and Cartwright, 2010). Although the 2D grid available here does not allow unequivocal demonstration of this geometry, the acoustic character in intersecting orthogonal 2D profiles is sufficient to interpret the features as fluid expulsion pipes by analogy with previously published examples (c.f. Cartwright et al. 2007; Andresen, 2012).

Fluid expulsion pipes can form in a number of different ways, including slow, focused fluid expulsion, rapid blow out of overpressured fluids or collapse due to subsurface dissolution (Cartwright et al. 2007). A rapid blow out mechanism is suggested wherever the upper termini of pipes form a pockmark crater (Løseth et al., 2011). Fluid expulsion pipes involving hydrocarbon fluids are recognised and distinguished by their association with amplitude anomaly trails along the pipe and in its immediate surrounding (Løseth et al. 2011; Moss et al. 2011). This diagnostic is important in the context of analysing a HPS because pipes can be associated with fluids other than hydrocarbons (Cartwright et al., 2007; Andresen, 2012).

Four pipes have been interpreted in the study area, and are all interpreted as having formed from focused fluid expulsion. The dimension of these pipes ranges approximately between 100–350 m in cross sectional width and 350–450 ms TWT in height. The pipes are distributed in the westernmost part of the basin in an area of 20×10 km (Figure 7B) and generally are found to occur closely to normal fault propagating from the acoustic basement. Two endmembers of these pipes, P1 and P2, are described here in detail (Figure 7).

P1 is contained entirely within Unit 2 (Figure 7). From the BSR to the seabed it can be described as a vertical zone of distorted and concave upward reflections with a maximum

intersected diameter of c.350m and a vertical extent of >400m. P1 is composed of 5 sections characterised by different cross sectional width and with non–coaxial geometry (black arrows, Figure 7D). This geometry, although observed in 2D cross section, may indicate multiple fluid expulsions (c.f. Andresen et al., 2011). P1 reaches the seabed and terminates at a large pockmark with a diameter of c.250m. The pipe is recognizable from the position of the BSR to the lower boundary of the enhanced reflections but is difficult to trace the feature any deeper due to imaging artefacts such as migration smiles. Hence the root zone of P1 cannot be located with any certainty (c.f. Moss et al., 2012).

Pipe P2 differs largely from P1 because of its narrow geometry. P2 is composed of a series of vertical quasi–resolvable stacked amplitude anomalies with a maximum width of 100m (Figure 7C). These anomalies stacked vertically are disposed axio–symmetrically. P2 terminates at the seabed in a small pockmark. P2 can be traced downwards as a vertical narrow zone of disrupted reflection continuity to approximately Horizon C (Figure 7C), where any further downward continuation is too weak to interpret confidently.

The pipes occur, in all the cases here observed, in a region containing basement–rooted normal faults (Figure 7B). Although the roots of the pipes are unclear, the pipes appear to coincide with the intersection of normal faults with the base of the ERs. The axis of P2 intersects a prominent normal fault at position R (Figure 7C). The intersection coincides also with the base of the ERs previously documented. The axis of P1 intersects a prominent normal fault at position R and R' (Figure 7D). Although the interpretation is here complicated by the lack of coherent reflections, the potential root of P1 (the midpoint between R and R') may coincide again at the base of the ERs. This observation suggests a relationship between the FGZ and the observed pipes (see Discussion).

The pipes discovered in Unit 2 are similar, in terms of geometry and acoustic characteristics, to those described by Gay et al. (2007) in Lower Congo Basin. In that example the pipes

represent focused fluid expulsions of mixed thermogenic and biogenic gases and oil. Similar columnar zones of disrupted or offset reflections have also been reported by Hustoft et al. (2009) in NW offshore Svalbard, Løseth et al. (2011) in offshore Nigeria, and Macelloni et al. (2012) in the Gulf of Mexico. All these cases indicate migration of hydrocarbon fluids from the subsurface to the seabed. The presence of pipes in the SMFB is strong evidence for fluid migration and expulsion and importantly they may potentially be associated with hydrocarbons (thermogenic or/and biogenic).

4.4. Vertical anomaly clusters (VACs)

Vertical anomaly clusters (VACs) can be observed on seismic data as an assemblage of discrete stacked amplitude anomalies which define a region of relative amplification but where the background reflectivity is clearly imaged and not distorted or strongly attenuated (Foschi et al., 2014). VACs are, by definition, related to the migration process which involves primarily hydrocarbons. A number of stacked amplitude anomalies that resemble the acoustic and the geometrical characteristics of VACs have been observed in the deeper section of Unit 2. Their description is based on two representative examples shown in Figure 8.

The first important characteristic of the observed stacked amplitude anomalies is that they differ from pipes because they are more broadly defined 'balloon' shaped regions within which the stacking of amplitude anomalies (AAs) is recognisable (Figure 8). The polarity of the AAs within VACs is negative with amplification from weak to moderate compared to the background amplitude values. The spaces between AAs exhibit zones of attenuation and loss of coherence which however do not prohibit the identification of the reflectivity structure (Figure 8). The lateral and vertical extent of the observed stacked AAs is hard to define due primarily to low amplification of some constituent AAs. Based on the best interpreted AAs a number of tentatively defined envelopes have been qualitatively constructed (e.g. VAC-1 and

2; Figure 8). The range size of the observed VACs exhibits an approximate width of 1-5 km and a vertical extent of 100–450 ms TWT. Some of the most prominent stacked AAs clearly terminate at the base of the ERs previously documented (VAC-1, Figure 8).

The observed stacked AAs are roughly rooted above relative shallowings of Horizon C and importantly above local structural highs and footwall crests of normal faults propagating from the acoustic basement (Horizon B, Figure 8). This observation points to a close relationship between the stacked amplitude anomalies and the deep structural elements of the basin. This point is discussed later.

Similar seismic features have been previously observed in other basins worldwide, including examples form North Sea Dutch sector (Van Den Boogaard and Hoetz, 2014) and from Sleipner underground CO_2 storage site (North Sea, Arts et al., 2004). Although these features may partially resemble more common seismic evidence of fluid migration, such as gas chimneys — where patchy gas saturation and intense fault networks heavily perturb the background reflectivity (e.g. Arntsen et al., 2007) — the clearer stacking of the amplitude anomalies and the relatively weak reflection disruptions observed here suggest to interpret the observed features as VACs. VACs have been described by Foschi et al (2014) 220km to NE in a shallower section of the East Malvinas/Falkland Basin (Figure 1A).

The lack of strong amplification in some of the observed stacked anomalies is potentially imputable to the depth of these features. The acoustic response of gas charged sediments decreases with depth due to a lower compressibility of the pore gas phases (Aveseth et al., 2009). For the same reason a number of gas charged layers could be virtually invisible below the interpreted base of these features. Also the presence of BSR and ERs above the VACs may have strongly attenuated the seismic signal, whitening the background reflectivity and the deeper amplitude anomalies.

4.5. Flat spots

Flat spots are the most definitive of all DHIs and represent the contact between two or more phases (e.g. gas and water, oil and water) separated by a horizontal interface with a positive acoustic impedance contrast (Brown, 2004). Flat spots are not always truly horizontal at depth and may be gently tilted because of reservoir hydrodynamics (England, 1987). They may appear tilted in a time section because of velocity effects (e.g. dipping seabed; Brown, 2004). One of the methods to corroborate the interpretation of flat spots as true DHIs is by the analysis of amplitude variation with offset (AVO). This analysis is crucial because pseudo flat spots may be generated by diagenetic boundaries characterised by a sharp increase of acoustic impedance with depth, such as Opal A–CT transitions (Neagu et al., 2010), or by sill intrusions (Planke et al.,2005) and channel lobes (Avseth et al., 2009).

A number of potential flat spots have been recognised in Unit 1b ranging in depth of 1–2 km below the seabed. They are mostly clearer in dip rather than strike profiles because they cross cut the southward dipping background reflectivity. They are generally of limited lateral extent (150–1600m) and associated with fault traps. They all occur to the northern regions of the study area.

A representative example of a flat spot within the survey area (FS1) is illustrated using two orthogonally intersecting seismic profiles (Figure 9A and B). FS1 exhibits a classical horizontal positive reflection (positive acoustic impedance contrast) (Figure 9A). FS1 is positioned directly beneath and truncates against a convex upward negative amplitude reflection. The discordant relationship between the flat spot and the stratigraphy is best seen in the dip section (Figure 9B), and thus represents strong evidence for a potential fluid contact (e.g. gas–water contact or oil–water contact). FS1 is laterally bounded by a northward dipping normal fault, which propagates from Horizon B to Horizon C (Figure 9B). The configuration of this flat spot

is therefore a classical fluid contact for a fault–dip petroleum trap (Gluyas and Swarbrick, 2003).

AVO analyses were conducted on the interpreted flat spots to further investigate the likelihood of them being true DHIs. In the analysed cases the results have been carefully interpreted due to the complexity of the geometry of the fault–traps and the potential contamination with lateral events within the AVO cross–plots.

Although the results show clearly AVO class IIn/III response for most of the observed flat spots in some cases the background response was dominant. AVO cross–plots in the example shown in Figure 9 are for FS1. Cross plots 1 and 2 exhibit a dominant background response located at the centre of the plot (at G=0; I=0), and anomalous trends are not observed. AVO cross–plot 3 shows again a dominant background trend but in this case a clear anomaly trend can be observed in the bottom left region of the cross–plot (3rd quadrant). The stronger response observed here and the clear separation of anomalous and background trend is consistent with a higher distance between top and base reflections of the interpreted reservoir interval. Following the classification of Castagna (1996) this result is associated with AVO class III response and consistent with the probable presence of compressible fluids, such as gas.

The presence of flat spots in the study area that exhibit Class III AVO anomalies is interpreted here as being most probably due to a free gas accumulation in a reservoir interval, with the flat spots being associated with gas/water contacts. The host stratigraphy of Unit 1 is interpreted as a fine grained clay–rich sequence with coarser layers embedded, by analogy with the unpublished results from the Darwin discovery well. This well is reported to have encountered a significant column of condensate at a depth of 2800m (from sea surface) which strengthens the interpretation proposed here that the observed flat spots are due to gas/water contacts, and furthermore suggests that the gas is thermogenic in origin (see Discussion).

5. Discussion

The previous sections document the presence of DHIs observed within the shallow and the deeper part of the basin, but the central question arising from these observations is whether or not these represent a connected HPS. A secondary question that has a strong bearing on the interpretation of these DHIs is whether the source of the hydrocarbons is biogenic, thermogenic or mixed origin. We tackle this question of source firstly, which, in the absence of direct sampling and geochemistry, is restricted to a purely qualitative assessment of the distribution of the DHIs with respect to the likely source units for biogenic versus thermogenic hydrocarbons (c.f. Andresen, 2012).

5.1 Biogenic hydrocarbon plumbing system

Biogenic methane is widely invoked to be the main constituent of the methane hydrates that are developed within the hydrate stability zone on many of the world's continental margin basins (e.g. Marchesi et al., 2000). Given that there is an extremely well developed BSR mappable over a large fraction of the study area, and given also that the seismic characteristics of this mapped BSR equate to those generally interpreted to form the BGSHZ, it might be reasonably assumed that such a laterally extensive hydrate deposit is far more likely to be fed from biogenic rather than thermogenic sources.

Biogenic methane is well known to be produced from moderately to highly organic rich sediments at depth ranges from the near surface up to in excess of 2000m below the seafloor, depending on the geothermal gradient (Rice, 1993). A typical ceiling value of 70° C is commonly assumed (e.g. Rice, 1993). Some studies suggest that biogenic gas generation requires a high sedimentation rate, above 50m/My – 200m/My (Pimmel and Claypool, 2001;

Clayton, 1992), a minimum of 0.5% of total organic carbon (TOC; Claypool and Kaplan, 1974), and a low–temperature and low–sulphate environment (Rice, 1993). Based on these parameters, it seems more likely that Unit 2 would be the host for any biogenic methane supplied to the modern hydrate reservoir, simply from its distribution and thickness pattern relative to the mapped BSR and associated ERs (Figure 5 and 6). Since Unit 2 is interpreted as Cenozoic in age, and deposited in largely deepwater sedimentary environments with a hemipelagic mode of sedimentation, it would seem most likely that the modern hydrate system would be derived from source units within Unit 2. However, caution is required in this argument: the lack of age calibration means that we cannot constrain the sedimentation rate in either Unit 1 or 2, and it is possible that Unit 1 also generated biogenic methane at some time in the past, when it was more shallowly buried.

Does the distribution of the BSR and associated ERs support the notion of a biogenic source? Although the BSR is mapped over a large portion of the basin and exclusively hosted in sediments of Unit 2 (Figures 4 and 5) and is related to the underlying ERs (Figure 6), there are large areas of the study area where both BSR and ERs are not developed at all (Figure 7). The irregular distribution of free gas in these ERs is puzzling if the gas is indeed biogenic methane, since there is nothing in the seismic facies to suggest anything other than laterally uniformity in the depositional facies within Unit 2. It is also difficult to explain this irregular distribution as being related to primary localisation of the generation of biogenic gas within the thickest part of the wedge and the subsequent migration to the observed sites of current accumulation because the dominantly lateral migration along strata within the wedge of Unit 2 would leave enough residual gas (e.g. Luo, 2011) to produce an appreciable amplitude amplification of the background reflectivity (Domenico, 1974) (Figure 7). Hence the absence of ERs instead suggests the complete absence of any migrated or reservoired methane. In summary, therefore,

the irregular distribution most probably points to some underlying focussing of the hydrocarbons into the shallowest part of the stratigraphy.

For the DHIs hosted in Unit 1, the question of a biogenic origin of any free–gas is even more difficult to consider. Unit 1 is largely buried beneath the accepted temperature ceiling for active methane generation so a biogenic origin would require early generation (during the Cretaceous), and retention of biogenic methane for tens of millions of years, which is difficult to reconcile with the long term impacts of gas diffusion (Hunt, 1984). More significantly, the reported discovery of gas condensate in the Darwin reservoir (2800m below seabed) implies a thermogenic source because of the presence of significant fraction of wet gases (e.g. Macelloni et al, 2012) (Figure 1).

5.2 Thermogenic hydrocarbons

The generation of petroleum fluids by thermal maturation of organic matter depends on a combination of temperature and burial history (depth and time; Selley, 1998). The presence of a proven petroleum system in the gas condensate of the Darwin discovery is strong evidence for the wider presence of thermogenic hydrocarbons within the basin, but could a simple thermogenic source explain the observed distribution of the mapped DHIs?

The Darwin discovery suggest mature source rocks at 3200m below the seabed (Figure 2DD), so to what extent could this source be more widely distributed, and could a deep 'kitchen' account for the basinwide extent of the DHIs? If so, what would this require in the way of a HPS to link the kitchen to the shallower hydrocarbon accumulations?

Source rock distribution

The source rock intervals of Oxfordian age encountered in the Darwin discovery well (Border & Southern, 2012a) are mostly embedded in Unit 1 and this interval is known to be widely distributed within the study area (Figure 2; Fish, 2005). In order to calculate the depth range of the potential generative kitchen, we depth converted a series of profiles close to the discovery well using a velocity field based on unpublished operator's reports and our own velocity analysis calculated from CDP gathers. Assuming that the Oxfordian organic–rich intervals are uniformly distributed within Unit 1a (Fish, 2005), we extended the 3200m contour through the basin fill and used this depth value as the upper limit of maturity. This also assumes a uniform burial history E–W along strike within the study area, which is reasonable given the similarity in thicknesses of Units 1 and 2 in the suite of N–S profiles. Based on this, the present day extent of the kitchen is an E–W trending elongate zone encompassing the southernmost flank of the basin, with a northern limit well to the south of the mapped extent of many of the DHIs (notably the four pipes, the ERs and the BSR) (Figure 10). This kitchen almost certainly extends to the south, beyond the mapped limits, and would be demarcated by the major fault bounding the Burdwood Bank. Loss of seismic imaging beneath the shallow structures comprising the Burdwood Bank preclude any more detailed interpretation, but the N–S profiles (e.g. Figure 2) show the monoclinally dipping flank containing the source interval dipping southwards at the position where the data are obscured, and projected depths of the source in this southern extremity would take this Oxfordian source rock well into the gas window. This deeper gas kitchen thus offers a simple explanation for the discovery of gas condensates in the Darwin reservoir.

Given the likely southerly restricted distribution of mature source rock depicted in Figure 10, how can we reconcile the distribution of DHIs in the northern part of the study area? In the south, the BSR and ERs are located directly above the mature source rock, so there is a requirement that for these to be sourced from depth, hydrocarbons would need to migrate

vertically to feed the shallow accumulations. In the north, the other DHIs lie outside the area of mature source rock; hence some component of stratal migration over length scales of tens of kilometres would be required along with vertical migration over distances of several thousands of metres. Thus we can infer that if all the DHIs are thermogenic in origin, some combination of stratal (along bedding) and cross–stratal (vertical) migration pathways must exist (c.f. England, 1987).

Stratal migration

From the limited data available from the Darwin discovery (well 61/17–1; Figure 2DD) and from seismic facies interpretation (Figures 2 and 4), it is highly likely that sand or silt–prone intervals occur within Units 1 and 2, although perhaps preferentially within Unit 1 (Fish, 2005; Platt and Philip, 1995) (Figure 2). These coarser intervals are probably thin, relative to the gross thickness of the predominately fine–grained succession comprising Unit 1b and Unit 2. These coarser sediments offer multiple potential stratal migration routes since from the seismic facies they are most likely to be uniformly distributed within the basin and are acoustically characterised by alternating low–high reflection amplitudes on seismic data (Figure 2).

Vertical migration (cross–stratal migration)

The most obvious routes for hydrocarbons to ascend to shallow levels in the basin are via the many faults that transect Unit 1, and to a lesser degree, Unit 2 (Figure 2). Faults are one of the three main groups of seal by–pass systems documented by Cartwright et al (2007). They may act as fluid conduits (Nunn, 1996, Capuano, 1993) but equally prevent the migration of fluids and hydrocarbons to the surface (Cartwright et al, 2007). Direct evidence for the role of faults as conduits for cross–stratal hydrocarbon migration is rare, and greater reliance is commonly placed on indirect observations such as stacked AAs clustered against faults (e.g.

Løseth et al, 2009). The observation in this study that many of the basement faults in the region were reactivated at some point during the Cenozoic as evidenced by their upward propagation above the major regional unconformity (Horizon C) and into Unit 2, enhances their potential as conduits since later reactivation is frequently associated with hydrocarbon leakage via fault networks (e.g. Fisher et al., 2001; Ilg et al., 2012; Ingram and Urai, 1999). Additional evidence that the basement faults played a role in vertical hydrocarbon migration comes from the observation of the close association between the pipes and the faults. The fact that the four mapped pipes are all located on footwall crests, close to reactivated normal faults is strong circumstantial evidence that there is a close link between pipe formation and fault activity, but the poor imaging of the deeper portions of the pipes prevents any strict causative connection being established. Furthermore, the striking overlap between regions of thickest ER development and major basement faults adds additional weight to the argument in favour of a fault control on vertical migration. The identification of flat spots in fault dip closures (Figure 9) demonstrates that there is effective trapping of hydrocarbons against some of the basement faults, so it can be concluded that not all the faults acted as vertical pathways. This duality of behaviour is frequently encountered in HPSs, where some faults act as valves and others as barriers to flow (Downey, 1984; Cartwright et al. 2007). We suggest therefore that it is the degree and timing of later reactivation that stimulated the change in behaviour from static seals or barriers to dynamic conduits (Sibson, 1990).

In summary, the evidence for the nature of the hydrocarbons in the study area overwhelmingly points to a deep thermogenic source, but a contribution from biogenic methane generated within Unit 2 in particular cannot be excluded. It seems reasonable to suggest therefore that a mixed, but dominantly thermogenic HPS is present in the study area (c.f. Gay et al., 2007; Shurr and Ridgley, 2002). Similar arguments have been presented to account for

hydrocarbon occurrences in the adjacent and structurally equivalent Malvinas basin, where shallow and deep DHIs have been attributed to gas of thermogenic origin (Baristeas et al., 2012).

5.3 Timing

The time of the emplacement of the observed DHIs is challenging to establish due to the lack of direct information about the expulsion of hydrocarbons from the source rocks or the timing of the migration processes (Moss and Cartwright, 2010). The presence of pockmarks at the seabed is the strongest indication that hydrocarbon migration was active at least within the recent past. Although difficult to demonstrate here, observations of pipes with similar dimensions in other petroliferous basins suggest that hydrocarbon discharge via pipe conduits is episodic and relatively long–lived (several millions of years) (Moss and Cartwright, 2010; Andresen and Huuse, 2011; Gay et al. 2012).

5.4. A model for the HPS in the South Falkland Basin

Based on the qualitative evaluations presented in the previous discussion we propose the following HPS for the SMFB (Figure 11) as a summary of the main findings of this study:

1. Hydrocarbons are generated from the Oxfordian mature source rock distributed in Unit 1. The generation of thermogenic hydrocarbons was demonstrated by the gas condensate discovery (Darwin).

2. The expelled hydrocarbon fluids migrate from the main kitchen areas in the southern flank of the basin northward, up–dip, by stratal migration along sand–rich layers mostly embedded in Unit 1b.

3. The basement normal faults propagating in Unit 1 act both as a barrier, generating fault related flat spots and also as vertical conduits transferring the hydrocarbons to the shallower Unit 2. The different modes of behaviour may be attributed to late stage reactivation and concomitant dilation of fault planes (c.f. Sibson, 1990).

4. Hydrocarbon migration produces the documented VACs, and the pipes in Unit 2. The close spatial relationship between pipes, major basement faults and footwall crests suggests some causative link, but this cannot be verified at present.

5. The lack of well calibration does not allow us to constrain the presence of biogenic gas in the basin, but from the patchy distribution of the BSR and associated ERs we consider that any contribution to a mixed hydrocarbon system is subordinate to the thermogenic flux.

6. Conclusions

Although the qualitative arguments proposed in the manuscript have to be verified with supportive quantitative analysis the following preliminary conclusions can be drawn:

1. The SMFB hosts a mature thermogenic source rock which is interpreted to be the major source of hydrocarbons in the study area.
2. The thermogenic hydrocarbon plumbing system exhibits a series of seismically recognizable amplitude anomalies that represent DHIs.
3. The DHIs are mostly consistent with thermogenic fluids. However biogenic gas can be produced and be contained in some concentration within the shallow gas hydrate system.
4. A number of Aptian sand–rich intervals and the Mesozoic basement normal fault system represent the dominant controls of the HPS.
5. The HPS inferred to be active at present due to the presence of seabed pockmarks.

Acknowledgments

The authors would like to thanks Paul Einarsson Chairman and COO of Geophysical Service Incorporated and Colin Moore of Falkland Oil and Gas Limited for providing academic access to seismic data. We thank BHP Billiton for sponsoring this project. We thank Schlumberger and Halliburton-Landmark ProMAX for providing software support. We thank Professor Bruce Levell, Dr. John Hooker and Professor Tony Watts for the constructive comments on this manuscript. We also thank Dr. P.R. Kress and Dr. A. Tassone for their reviews and comments. The industry seismic data shown in the manuscript (Figures 2, 3, 4, 6, 7, 8 and 9) is currently proprietary. The industry's press releases related to the well 61/17–1 (RNS Number: 8142B and 6716K) are available on the Border & Southern Petroleum plc website (http://www.bordersandsouthern.com/).

References

Andresen, K. J. (2012), Fluid flow features in hydrocarbon plumbing systems: What do they tell us about the basin evolution?, Marine Geology, 332–334, 89–108.

Andresen, K. J., and M. Huuse (2011), 'Bulls–eye' pockmarks and polygonal faulting in the Lower Congo Basin: Relative timing and implications for fluid expulsion during shallow burial, Marine Geology, 279(1–4), 111–127.

Anka, Z., C. Berndt, and A. Gay (2012), Hydrocarbon leakage through focused fluid flow systems in continental margins, Marine Geology, 332–334, 1–3.

Aplin, A. C., A. J. Fleet, and J. H. S. Macquaker (1999), Muds and mudstones: physical and fluid–flow properties, Geological Society, London, Special Publications, 158(1), 1–8.

Arntsen, B., L. Wensaas, H. Løseth, and C. Hermanrud (2007), Seismic modeling of gas chimneys, Geophysics, 72(5), 251–259.

Arts, R., O. Eiken, A. Chadwick, P. Zweigel, B. van der Meer, and G. Kirby (2004), Seismic monitoring at the Sleipner underground CO 2 storage site (North Sea), edited, pp. 181–191.

Avseth, P., T. Mukerji, and G. Mavko (2009), Quantitative Seismic Interpretation. Applying Rock Physics to Reduce Interpretation Risk, Cambridge University Press, Cambridge.

Baristeas, N., Z. Anka, R. di Primio, J. F. Rodriguez, D. Marchal, and F. Dominguez (2012), Distribution of hydrocarbon leakage indicators in the Malvinas Basin, offshore Argentine continental margin, Marine Geology, 332–334, 56–74.

Baristeas, N., Anka, Z., di Primio, R., Rodriguez, J.F., Marchal, D., Dominguez, F., 2013. New insights into the tectono-stratigraphic evolution of the Malvinas Basin, offshore of the southernmost Argentinean continental margin. Tectonophysics 604, 280-295.

Barker, P. F. (2001). "Evolution of the Scotia Sea region: Relevance to broad-band seismology." Terra Antarctica 8(1-2): 67-70.

Berndt, C. (2005), Focused fluid flow in passive continental margins, Philosophical Transactions of the Royal Society A: Mathematical, Physical and Engineering Sciences, 363(1837), 2855–2871.

Borders & Southern (2012a), 61/17–1 (Darwin East) Well Result, RNS Number: 8142B (http://www.bordersandsouthern.com/news/rns_viewer.php?id=20044683)

Borders & Southern (2012b), Darwin Fluid Analysis, RNS Number: 6716K (http://www.bordersandsouthern.com/news/rns_viewer.php?id=20315808)

Brooks, J. M., M. E. Field, and M. C. Kennicutt Ii (1991), Observations of gas hydrates in marine sediments, offshore northern California, Marine Geology, 96(1–2), 103–109.

Brown, A. R. (2004), Interpretation of Three–Dimensional Seismic Data, 6 ed., AAPG.

Bry, M., N. White, S. Singh, R. England, and C. Trowell (2004), Anatomy and formation of oblique continental collision: South Falkland basin, Tectonics, 23(4), TC4011 4011–4020.

Bull, S., J. Cartwright, and M. Huuse (2009), A review of kinematic indicators from mass–transport complexes using 3D seismic data, Marine and Petroleum Geology, 26(7), 1132–1151.

Bünz, S., J. Mienert, and C. Berndt (2003), Geological controls on the Storegga gas–hydrate system of the mid–Norwegian continental margin, Earth and Planetary Science Letters, 209(3–4), 291–307.

Calvès, G., M. Huuse, A. Schwab, and P. Clift (2008), Three–dimensional seismic analysis of high–amplitude anomalies in the shallow subsurface of the northern Indus Fan: Sedimentary and/or fluid origin, Journal of Geophysical Research B: Solid Earth, 113(11).

Capuano, R. M. (1993), Evidence of fluid flow in microfractures in geopressured shales, American Association of Petroleum Geologists Bulletin, 77(8), 1303–1314.

Cartwright, A., J. Moss, and J. Cartwright (2011), New statistical methods for investigating submarine pockmarks, Computers and Geosciences, 37(10), 1595–1601.

Cartwright, J., M. Huuse, and A. Aplin (2007), Seal bypass systems, AAPG Bulletin, 91(8), 1141–1166.

Castagna, J. P., and S. W. Smith (1994), Comparison of AVO indicators: a modeling study, Geophysics, 59(12), 1849–1855.

Castagna, J. P., and H. W. Swan (1997), Principles of AVO crossplotting, Leading Edge (Tulsa, OK), 16(4), 337.

Claypool, G., and I. R. Kaplan (1974), The Origin and Distribution of Methane in Marine Sediments, in Natural Gases in Marine Sediments, edited by I. Kaplan, pp. 99–139, Springer US.

Clayton, C. (1992), Source volumetrics of biogenic gas generation, Bacterial gas. Proc. conference, Milan, 1989, 191–204.

Cukur, D., S. Krastel, Y. Tomonaga, M. N. Çağatay, and A. F. Meydan (2013), Seismic evidence of shallow gas from Lake Van, eastern Turkey, Marine and Petroleum Geology, 48, 341–353.

Cunningham, A. P., J. A. Howe, and P. F. Barker (2002), Contourite sedimentation in the Falkland Trough, western South Atlantic, Geological Society, London, Memoirs, 22(1), 337–352.

Dalziel, I. W. D., et al. (2013). The Scotia arc: Genesis, evolution, global significance. Annual Review of Earth and Planetary Sciences. 41: 767-793.

Davison, I. (1999). Tectonics and hydrocarbon distribution along the Brazilian South Atlantic margin. Geological Society Special Publication. 153: 133-151.

Del Ben, A. and A. Mallardi (2004). "Interpretation and chronostratigraphic mapping of multichannel seismic reflection profile I95167, Eastern Falkland Plateau (South Atlantic)." Marine Geology 209(1-4): 347-361.

Domenico, S. (1974), Effect of water saturation on seismic reflectivity of sand reservoirs encased in shale, geophysics, 39(6), 759–769.

Downey, M. W. (1984), Evaluating seals for hydrocarbon accumulations, American Association of Petroleum Geologists Bulletin, 68(11), 1752–1763.

Dullien, F. A. (2012), Porous media: fluid transport and pore structure, Academic press.

Ecker, C., J. Dvorkin, and A. Nur (1998), Sediments with gas hydrates: Internal structure from seismic AVO, Geophysics, 63(5), 1659–1669.

England, W. A., A. S. Mackenzie, D. M. Mann, and T. M. Quigley (1987), The movement and entrapment of petroleum fluids in the subsurface, Journal of the Geological Society, 144(2), 327–347.

Esteban, F. D., Tassone, A., Lodolo, E., and M. Menichetti (2013), Structural setting of the western South America-Scotia plate boundary, proceeding of The Scotia Arc: Geodynamic Evolution & Global Implications.

Fish, P. (2005), Frontier South, East Falkland basins reveal important exploration potential, Oil and Gas Journal, 45(103), 34–40.

Fisher, Q. J., S. D. Harris, E. McAllister, R. J. Knipe, and A. J. Bolton (2001), Hydrocarbon flow across faults by capillary leakage revisited, Marine and Petroleum Geology, 18(2), 251–257.

Fohrmann, M., and I. A. Pecher (2012), Analysing sand–dominated channel systems for potential gas–hydrate–reservoirs using an AVO seismic inversion technique on the Southern Hikurangi Margin, New Zealand, Marine and Petroleum Geology, 38(1), 19–34.

Foschi, M., J. A. Cartwright, and F. J. Peel (2014), Vertical anomaly clusters: Evidence for vertical gas migration across multilayered sealing sequences, AAPG Bulletin, 98(9), 1859–1884.

Frey–Martínez, J. (2010), 3D Seismic Interpretation of Mass Transport Deposits: Implications for Basin Analysis and Geohazard Evaluation, in Submarine Mass Movements and

Their Consequences, edited by D. Mosher, R. C. Shipp, L. Moscardelli, J. Chaytor, C. P. Baxter, H. Lee and R. Urgeles, pp. 553–568, Springer Netherlands.

Galeazzi, J. S. (1998), Structural and Stratigraphic Evolution of the Western Malvinas Basin, Argentina, AAPG Bulletin, 82(4), 596–636.

Gay, A., M. Lopez, C. Berndt, and M. Séranne (2007), Geological controls on focused fluid flow associated with seafloor seeps in the Lower Congo Basin, Marine Geology, 244(1–4), 68–92.

Gay, A., R. Mourgues, C. Berndt, D. Bureau, S. Planke, D. Laurent, S. Gautier, C. Lauer, and D. Loggia (2012), Anatomy of a fluid pipe in the Norway Basin: Initiation, propagation and 3D shape, Marine Geology, 332–334, 75–88.

Ghiglione, M.C., Quinteros, J., Yagupsky, D., Bonillo-Martínez, P., Hlebszevtich, J., Ramos, V.A., Vergani, G., Figueroa, D., Quesada, S., Zapata, y.T., 2010. Structure and tectonic history of the foreland basins of southernmost South America. Journal of South American Earth Sciences 29, 262-277.

Gluyas, J., and R. Swarbrick (2003), Petroleum geoscience, Petroleum Geoscience, 9(4), 1–349.

Helgerud, M. B., J. Dvorkin, A. Nur, A. Sakai, and T. Collett (1999), Elastic–wave velocity in marine sediments with gas hydrates: Effective medium modeling, Geophysical Research Letters, 26(13), 2021–2024.

Holbrook, W. S., H. Hoskins, W. T. Wood, R. A. Stephen, and D. Lizarralde (1996), Methane hydrate and free gas on the Blake Ridge from vertical seismic profiling, Science, 273(5283), 1840–1843.

Hunt, J. M. (1984), Generation and migration of light hydrocarbons, Science, 226(4680), 1265–1270

Hustoft, S., J. Mienert, S. Bünz, and H. Nouzé (2007), High–resolution 3D–seismic data indicate focussed fluid migration pathways above polygonal fault systems of the mid–Norwegian margin, Marine Geology, 245(1–4), 89–106.

Hustoft, S., S. Bünz, J. Mienert, and S. Chand (2009), Gas hydrate reservoir and active methane–venting province in sediments on < 20 Ma young oceanic crust in the Fram Strait, offshore NW–Svalbard, Earth and Planetary Science Letters, 284(1–2), 12–24.

Ilg, B. R., S. Hemmings–Sykes, A. Nicol, J. Baur, M. Fohrmann, R. Funnell, and M. Milner (2012), Normal faults and gas migration in an active plate boundary, southernTaranaki Basin, offshore New Zealand, AAPG Bulletin, 96(9), 1733–1756.

Imbert, P. (2009), Seismic–scale expression of fluid sourcing, circulation and expulsion in sedimentary series, paper presented at Society of Petroleum Engineers – International Petroleum Technology Conference 2009, IPTC 2009.

Ingram, G. M., and J. L. Urai (1999), Top–seal leakage through faults and fractures: the role of mudrock properties, edited, pp. 125–135.

Koenitz, D., et al. (2008). "Internal structure of a contourite drift generated by the Antarctic Circumpolar Current." Geochemistry, Geophysics, Geosystems 9(6).

Koltermann, C. E., and S. M. Gorelick (1995), Fractional packing model for hydraulic conductivity derived from sediment mixtures, Water Resources Research, 31(12), 3283–3297.

Korenaga, J., W. S. Holbrook, S. C. Singh, and T. A. Minshull (1997), Natural gas hydrates on the southeast U.S. margin: Constraints from full waveform and travel time inversions of wide–angle seismic data, Journal of Geophysical Research B: Solid Earth, 102(B7), 15345–15365.

Li, L., X. Lei, X. Zhang, and Z. Sha (2013), Gas hydrate and associated free gas in the Dongsha Area of northern South China Sea, Marine and Petroleum Geology, 39(1), 92–101.

Liu, X., and P. B. Flemings (2007), Dynamic multiphase flow model of hydrate formation in marine sediments, Journal of Geophysical Research B: Solid Earth, 112(3).

Løseth, H., M. Gading, and L. Wensaas (2009), Hydrocarbon leakage interpreted on seismic data, Marine and Petroleum Geology, 26(7), 1304–1319.

Løseth, H., L. Wensaas, B. Arntsen, N. M. Hanken, C. Basire, and K. Graue (2011), 1000 m long gas blow–out pipes, Marine and Petroleum Geology, 28(5), 1040–1060.

Ludwig, W. J. (1983), Geologic framework of the Falkland Plateau, Initial reports DSDP, Leg 71, Valparaiso to Santos, 1980, part 1, 281–293.

Luo, X. (2011), Simulation and characterization of pathway heterogeneity of secondary hydrocarbon migration, AAPG Bulletin, 95(6), 881–898.

Macdonald, D., et al. (2003). "Mesozoic break-up of SW Gondwana: Implications for regional hydrocarbon potential of the southern South Atlantic." Marine and Petroleum Geology 20(3-4): 287-308.

Macelloni, L., A. Simonetti, J. H. Knapp, C. C. Knapp, C. B. Lutken, and L. L. Lapham (2012), Multiple resolution seismic imaging of a shallow hydrocarbon plumbing system, Woolsey Mound, Northern Gulf of Mexico, Marine and Petroleum Geology, 38(1), 128–142.

Marchesi, J. R., A. J. Weightman, B. A. Cragg, R. John Parkes, and J. C. Fry (2000), Methanogen and bacterial diversity and distribution in deep gas hydrate sediments from

the Cascadia Margin as revealed by 16S rRNA molecular analysis, FEMS Microbiology Ecology, 34(3), 221–228.

Morley, C. K., R. King, R. Hillis, M. Tingay, and G. Backe (2011), Deepwater fold and thrust belt classification, tectonics, structure and hydrocarbon prospectivity: A review, Earth–Science Reviews, 104(1–3), 41–91.

Moss, J. L., and J. Cartwright (2010), 3D seismic expression of km–scale fluid escape pipes from offshore Namibia, Basin Research, 22(4), 481–501.

Moss, J. L., J. Cartwright, A. Cartwright, and R. Moore (2012), The spatial pattern and drainage cell characteristics of a pockmark field, Nile Deep Sea Fan, Marine and Petroleum Geology, 35(1), 321–336.

Neagu, R. C., J. Cartwright, and R. Davies (2010), Measurement of diagenetic compaction strain from quantitative analysis of fault plane dip, Journal of Structural Geology, 32(5), 641–655.

Nunn, J. A. (1996), Buoyancy–driven propagation of isolated fluid–filled fractures: Implications for fluid transport in Gulf of Mexico geopressured sediments, Journal of Geophysical Research: Solid Earth, 101(B2), 2963–2970.

Ostanin, I., Z. Anka, R. di Primio, and A. Bernal (2013), Hydrocarbon plumbing systems above the Snøhvit gas field: Structural control and implications for thermogenic methane leakage in the Hammerfest Basin, SW Barents Sea, Marine and Petroleum Geology, 43, 127–1

Pimmel, A., and G. Claypool (2001), Introduction to shipboard organic geochemistry on the JOIDES Resolution, ODP Tech. Note, 30, 1–29.

Planke, S., T. Rasmussen, S. S. Rey, and R. Myklebust (2005), Seismic characteristics and distribution of volcanic intrusions and hydrothermal vent complexes in the Vøring and Møre basins, in Petroleum Geology Conference Proceedings, edited, pp. 833–844.

Platt, N. H., and P. R. Philip (1995), Structure of the southern Falkland Islands continental shelf: initial results from new seismic data, Marine and Petroleum Geology, 12(7), 759–771.

Pucci, J. C. (2006), Southern offshore basins of Argentina underexplored, Oil and Gas Journal, 104(12), 30–33.

Rice, D. D. (1993), Biogenic gas: Controls, habitats, and resource potential, Journal Name: United States Geological Survey, Professional Paper; (United States); Journal Volume: 1570, Medium: X; Size: Pages: 583–606.

Richards, P. C., R. W. Gatliff, M. F. Quinn, J. P. Williamson, and N. G. T. Fannin (1996), The geological evolution of the Falkland Islands continental shelf, edited, pp. 105–128.

Satyavani, N., N. K. Thakur, U. Shankar, S. I. Reddi, A. R. Sridhar, P. Prasada Rao, K. Sain, and R. Khanna (2003), Indicators of gas hydrates: Role of velocity and amplitude, Current Science, 85(9), 1360–1363.

Selley, R. C. (1998), Elements of Petroleum Geology, Academic Press.

Shelander, D., J. Dai, G. Bunge, S. Singh, M. Eissa, and K. Fisher (2012), Estimating saturation of gas hydrates using conventional 3D seismic data, Gulf of Mexico Joint Industry Project Leg II, Marine and Petroleum Geology, 34(1), 96–110.

Shurr, G. W., and J. L. Ridgley (2002), Unconventional shallow biogenic gas systems, American Association of Petroleum Geologists Bulletin, 86(11), 1939–1969.

Sibson, R. H. (1990), Conditions for fault–valve behaviour, Geological Society, London, Special Publications, 54(1), 15–28.

Stone, P., et al. (2009). "Rotation of the Falklands microplate reassessed after recognition of discrete Jurassic and Cretaceous dyke swarms." Petroleum Geoscience 15(3): 279-287.

Sun, Y., S. Wu, D. Dong, T. Lüdmann, and Y. Gong (2012), Gas hydrates associated with gas chimneys in fine–grained sediments of the northern South China Sea, Marine Geology, 311–314, 32–40.

Tassone, A., et al. (2008). "Seismostratigraphic and structural setting of the Malvinas Basin and its southern margin (Tierra del fuego Atlantic offshore)." Geologica Acta 6(1): 55-67.

Tinivella, U., and M. Giustiniani (2013), Variations in BSR depth due to gas hydrate stability versus pore pressure, Global and Planetary Change, 100(0), 119–128.

Van Den Boogaard, M., and G. Hoetz (2014), Derisking shallow gas as exploration target by seismic characterisation, paper presented at Shallow Anomalies Workshop: Indications of Prospective Petroleum Systems?

Watts, A. B., and W. B. F. Ryan (1976), Flexure of the lithosphere and continental margin basins, Tectonophysics, 36(1–3), 25–44.

Vérard, C., et al. (2012). "Geodynamic reconstructions of the South America-Antarctica plate system." Journal of Geodynamics 53(1): 43-60.

Widess, M. (1973), How thin is a bed?, Geophysics, 38(6), 1176–1180.

Wood, W. T., and C. Ruppel (2000), Seismic and thermal investigations of the Blake Ridge gas hydrate area: A synthesis, Proceedings of the Ocean Drilling Program: Scientific Results, 164, 253–264.

Yoo, D. G., N. K. Kang, B. Y. Yi, G. Y. Kim, B. J. Ryu, K. Lee, G. H. Lee, and M. Riedel (2013), Occurrence and seismic characteristics of gas hydrate in the Ulleung Basin, East Sea, Marine and Petroleum Geology, 47(0), 236–247.

Figure 1. Location map of the Malvinas/Falkland Islands and surrounding basins with main tectonic elements, distribution of the Mesozoic–Cenozoic sedimentary coverage (grey shade, dashed lines) and contouring of the bathymetry @ 1300 ms TWT (dotted line; A; from Platt and Philip, 1995 (mod.)). The South Malvinas/Falkland Basin (SM/FB) is located approximately 200 km south of the Malvinas/Falkland Islands. NM/FB=North Malvinas/Falkland Basin, EM/FB=East Malvinas/Falkland Basin. Detailed bathymetric map of the seabed (derived from seismic interpretation), 2D seismic grid, well site 61/17–1 location, and main structural elements of the SM/FB (B). The SM/FB runs along the Scotia–South America Plate Boundary which divides the South America Plate and the Scotia Plate (B). The seabed plunges eastward with a maximum depth of c.2000m close to the position of the well site 61/17–1 and a minimum depth of 140m above the Burdwood Bank (B).

Figure 2. Representative 2D dip section (depth converted) crossing the South Falkland basin, with interpretation of the main structural elements and horizons, and position of the well 61/17–1 (projected, AA). The basement normal faults to the centre–north region and the thrust–fold belt anticline system to the south dominate the structural setting of the basin (AA). B=acoustic basement. C=Upper Cretaceous Unconformity. Representative basement normal faults interpreted on a close–up (BB) of the 2D dip section (AA). Depth–throw cross plot (depth-normalised at Horizon C) of the normal faults interpreted in close–up BB (CC, colour–coded). The cross plot shows that the basement normal faults were active mostly in the Mesozoic. Representative close–up of the stratigraphic package (DD) and previously reported stratigraphic columns (from Fish, 2005 (mod.), and Platt and Philip, 1995 (mod.)) used to characterise the lithostratigraphy of the defined units and synthesis of Darwin well (qualitative correlation). The sedimentary package is mostly composed of fine grained sediments. Unit 1b exhibits a number intervals characterised by coarse sediments, such as silt and sandstone. Springhill formation sand member is comparable to Darwin reservoir (DD). The Darwin well exhibits multiple immature source intervals (green shade, DD) reported to be Aptian in age. The Darwin reservoir (Aptian) is mostly composed of sand and with a net pay interval of 67.8m. Gas condensate (47°API) has been recovered during the drilling operations. Unpenetrated mature source rock are present 320 m below the base of the well (TD = 4876 m; C).

Figure 3. 2D cross section depicting the Bottom Simulating Reflection (BSR, A, see Figure 1 for location). Traces T1 to T5 are plotted in wiggle display. The BSR exhibits systematic negative amplitude response. High amplitude anomalies in T1 are related to enhanced

reflections (described later). In T2, T3 and T4 the BSR shows the strongest amplitude response. Weak, but still negative, response is observed in the southern regions within the thrust–fold belt system (T5).

Figure 4. Map of the interpreted Bottom Simulating Reflection (BSR) amplitude anomalies and their expression on 2D cross sections. The BSR exhibits different continuity on map view (A; see Figure 1 for location). Regions of high continuity (HC) are observed to the north and to the south of the BSR distribution. Patchily distribution of the BSR (PD) is mostly observed at the centre of the basin. The BSR is mostly visible when the reflectivity and the seabed have divergent geometry (B, C, DS). The interpretation of the BSR is challenging where the stratigraphy is parallel to the seabed however it is easily interpreted within Mass Transport Deposit (MTDs; DN).

Figure 5. Distribution and morphology of the Bottom Simulating Reflection (BSR; see Figure 1 for location of the map), contour of the seabed and structural elements (A). To the North the morphology of the BSR (A) exhibits a nonlinear trend with respect of the seabed as evidenced by crossing of the contour lines (CC) of the interpreted surfaces. Domal–shallowing of the BSR (DSB; B) are also present to NW (C). To the South the BSR and the seabed shapes are parallel to each other as highlighted by parallel contours (PC).

Figure 6. Representative 2D dip section depicting a package of Enhanced reflections (ER, ERs) here interpreted as a free–gas zone located beneath the Bottom Simulating Reflection (BSR; A, see Figure 6D for location). The ERs are often composed by amplified positive-negative loops may related to the top and the base of the layers close or below tuning thickness (B). The free–gas zone (FGZ) is limited at the top by the BSR, and by an interpreted base of the FGZ (BFGZ) at the base. The BSR exhibits a "roof–tile" configuration due to the discordant stratigraphy of the host (C). Time–thickness map of the FGZ in the study area (D, see Figure 1 for location of the map). The FGZ is mostly distributed in the northern regions which are also characterised by denser normal faulting. Poor to null distribution of free gas within the central regions. B=acoustic basement. C=Upper Cretaceous Unconformity.

Figure 7. 2D seismic dip transecting pipes P1 and P2, and interpretation of the main structural features and horizons (A, see Figure 7B for location). The pipes are located in proximity of foot wall crests of basement normal faults and where the Bottom Simulating Reflection (BSR)

exhibits domal shallowing (DSB, A). Location map of the discovered pipes with contouring and dip map of the BSR (B, see Figure 1 for location of the map). All the pipes discovered are located in the proximity of 1) basement normal faults and 2) within domal-shallowing of the BSR. Close–ups depicting pipe P1 (D) and P2 (C). Pipe P2 axis coincides with a basement normal fault in R at the base of the enhanced reflections (Base ERs, C). Pipe P1 axis intersects a number of interpreted normal faults within the depth range R–R'(D). Pipe P1 exhibits non–coaxial geometry (black arrows). Question marks represent uncertain interpretations. B=acoustic basement. C=Upper Cretaceous Unconformity.

Figure 8. Representative 2D dip sections depicting stacked amplitude anomalies here interpreted as vertical anomaly clusters (VAC, see Figure 1 for location). The VACs are systematically located above prominent structural shallows of the basement (Horizon B). These regions are characterised by moderate faulting which propagate to the shallower intervals and over Horizon C. The dimension of the VACs is based on the constituent amplitude anomalies (AA). VAC-1 clearly merges into the stacked enhanced reflections (ER). B=acoustic basement. C=Upper Cretaceous Unconformity.

Figure 9. Orthogonal 2D seismic sections depicting a flat spot (FS; see Figure 1 for location). The FS occurs entirely in Unit 1 and comprised within Horizon B and B1. The top structure is approximately consistent with Horizon B1. AVO analyses of 3 representative windowed regions intersecting the flat spot in different portions (lateral to central). Striking AVO class III response in AVO Crossplot–3. B=acoustic basement. B1=horizon separating sub-units 1a and b. C=Upper Cretaceous Unconformity.

Figure 10. Distribution of gas hydrate system (bottom simulating reflection, BSR, and free gas zone, FGZ), direct hydrocarbon indicators (DHIs), structural elements of the basin and distribution of the computed mature source rock embedded within Unit 1 (see Figure 1 for location of the map). The DHIs are in most of the cases located closely to basement normal faults. No DHIs have been observed directly above the source rock (SR). VAC=vertical anomaly cluster.

Figure 11. Conceptual model of the hydrocarbon plumbing system active in the South Malvinas/Falkland Basin. The mature source rock is expected to be present below 3200m (red dashed line). From the source rock at the base of the basin to the seabed the following features

are observed: flat-spots (FS), vertical anomaly clusters (VAC), free-gas zone (FGZ), bottom simulating reflection (BSR) and pipes. B=acoustic basement. C=Upper Cretaceous Unconformity. See text for further explanations.

Figure 1.

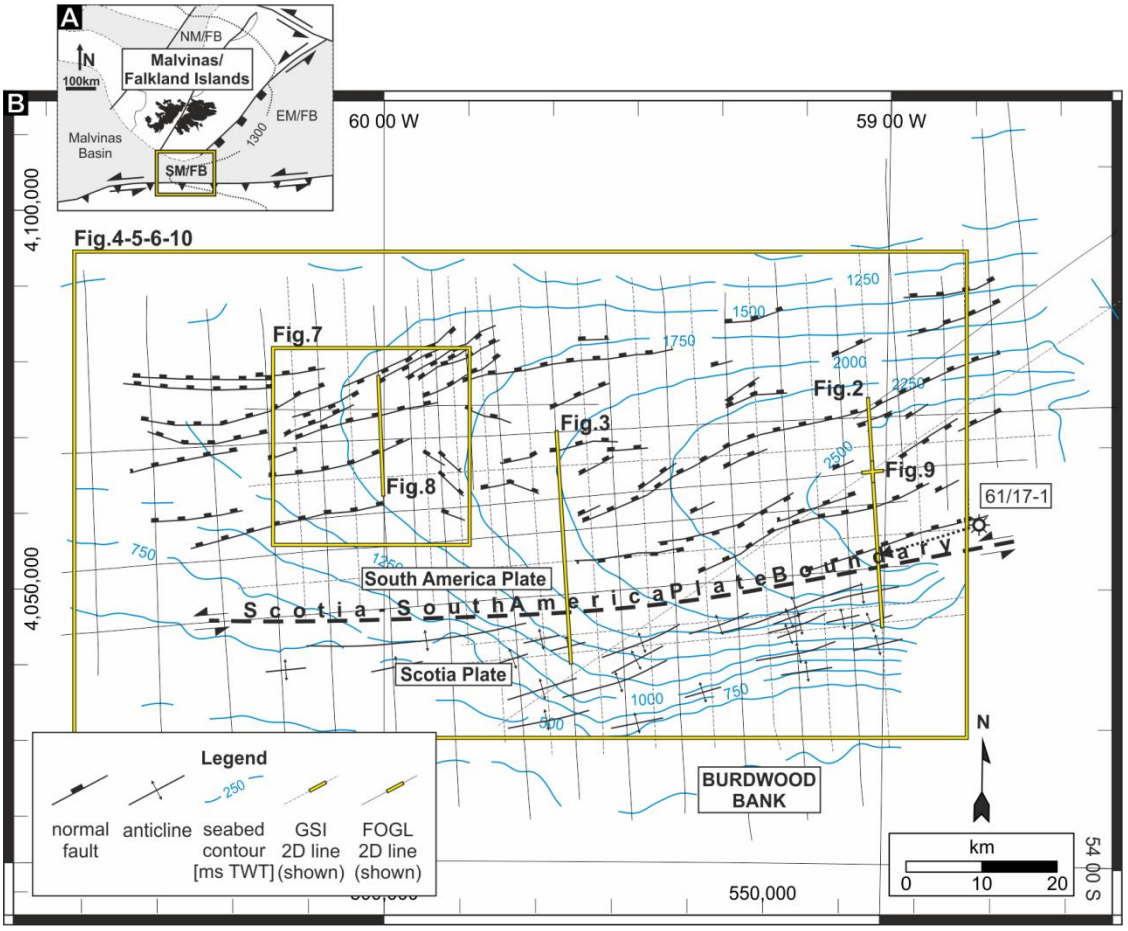
A
NM/FB
N
100km
Malvinas/
Falkland Islands
EM/FB
1300
Malvinas
Basin
SM/FB
B
60 00 W
59 00 W
4,100,000
4,050,000
Fig.4-5-6-10
Fig.7
Fig.8
Fig.3
Fig.2
Fig.9
61/17-1
1250
1500
1750
2000
2250
2500
750
1000
500
South America Plate
Scotia-SouthAmericaPlateBoundary
Scotia Plate
BURDWOOD
BANK
Legend
normal fault
anticline
250
seabed contour [ms TWT]
GSI 2D line (shown)
FOGL 2D line (shown)
N
km
0
10
20
550,000
54 00 S

Figure 2.

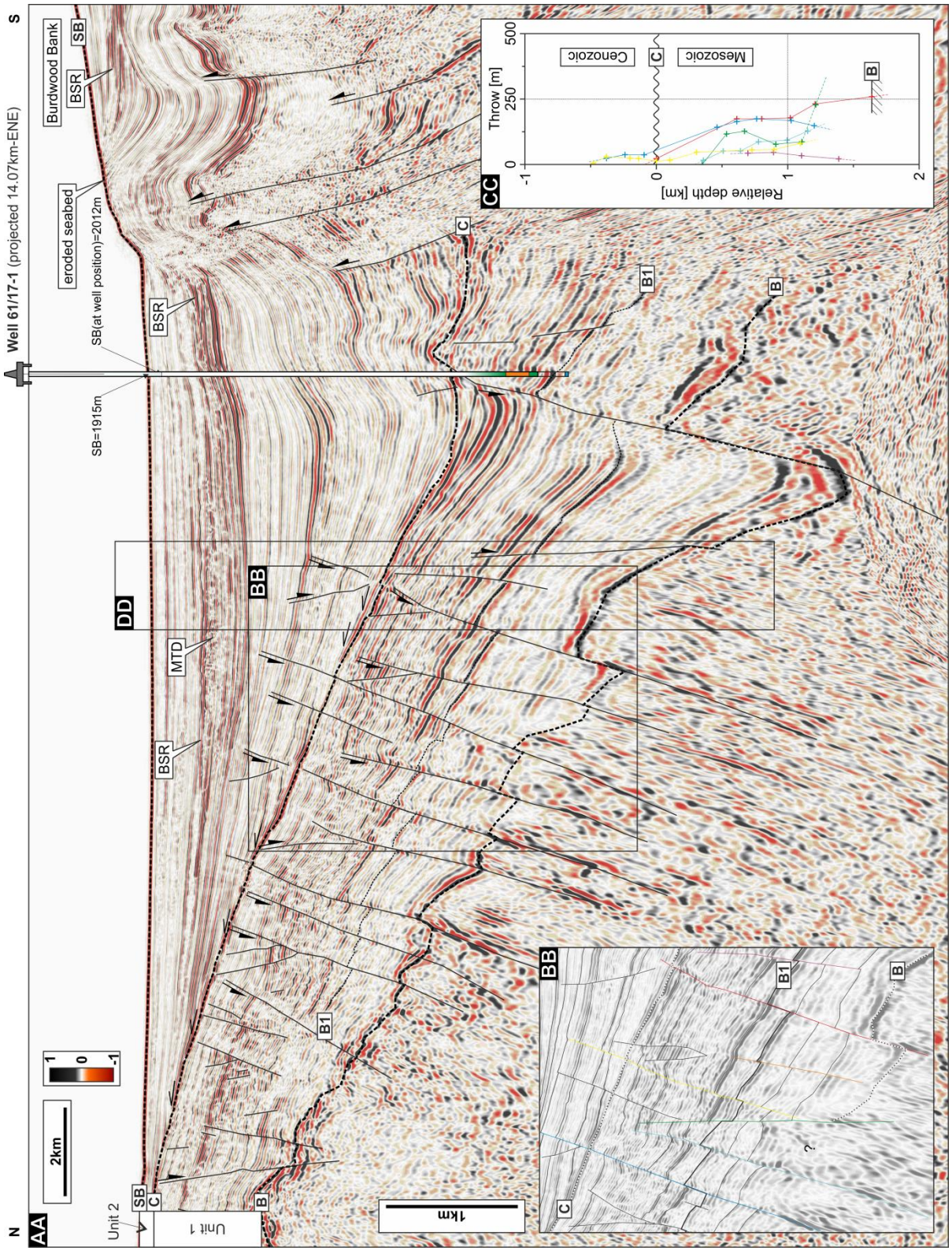
N
S
AA
Well 61/17-1 (projected 14.07km-ENE)
Burdwood Bank
BSR
SB
eroded seabed
SB(at well position)=2012m
SB=1915m
BSR
C
B1
B
DD
BB
MTD
BSR
2km
1
0
-1
Unit 2
Unit 1
SB
C
B
1km
BB
B1
B
C
?
CC
Throw [m]
500
250
0
Cenozoic
Mesozoic
C
B
-1
0
1
2
Relative depth [km]

Figure 2 (continue).

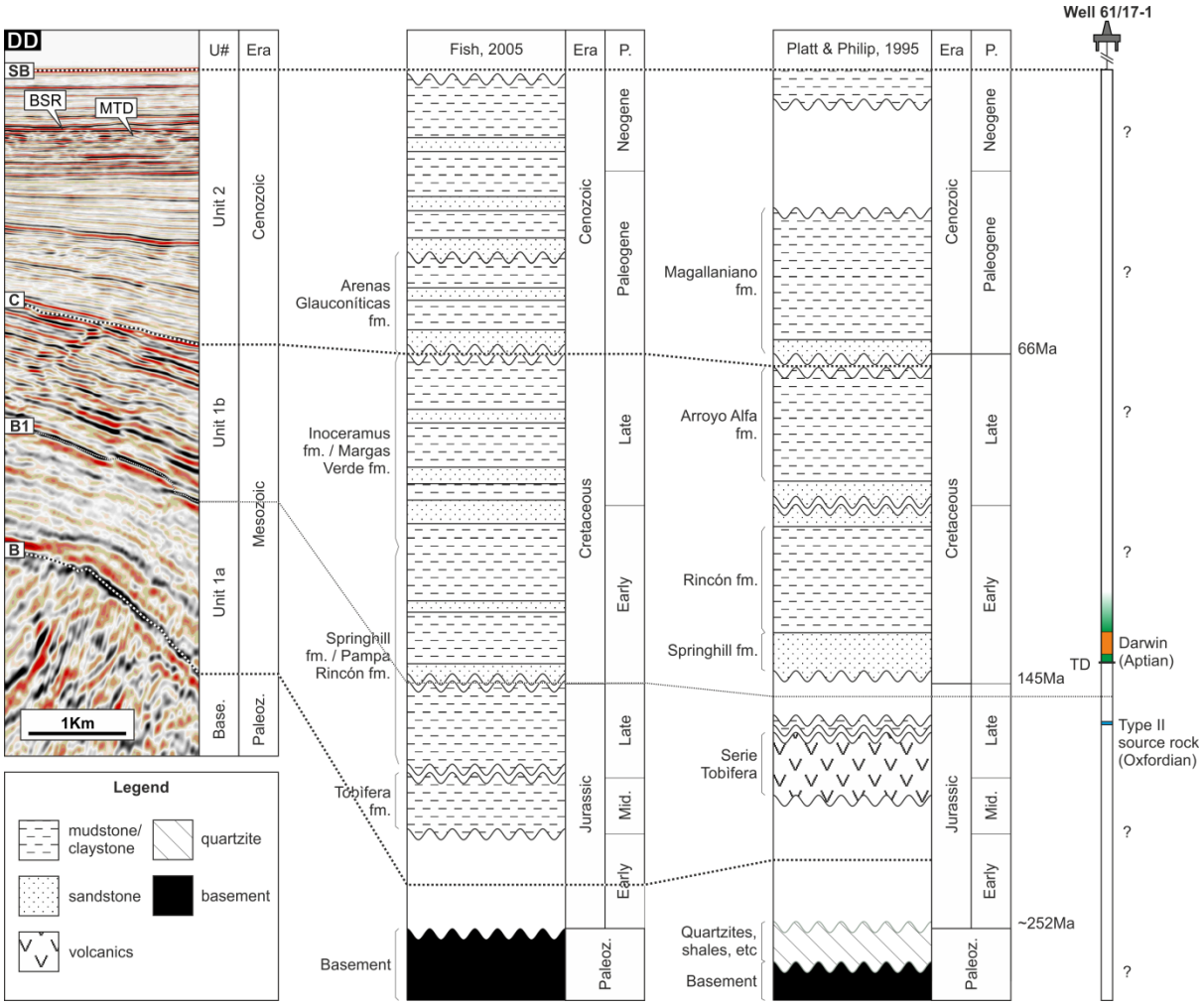

Figure 3.

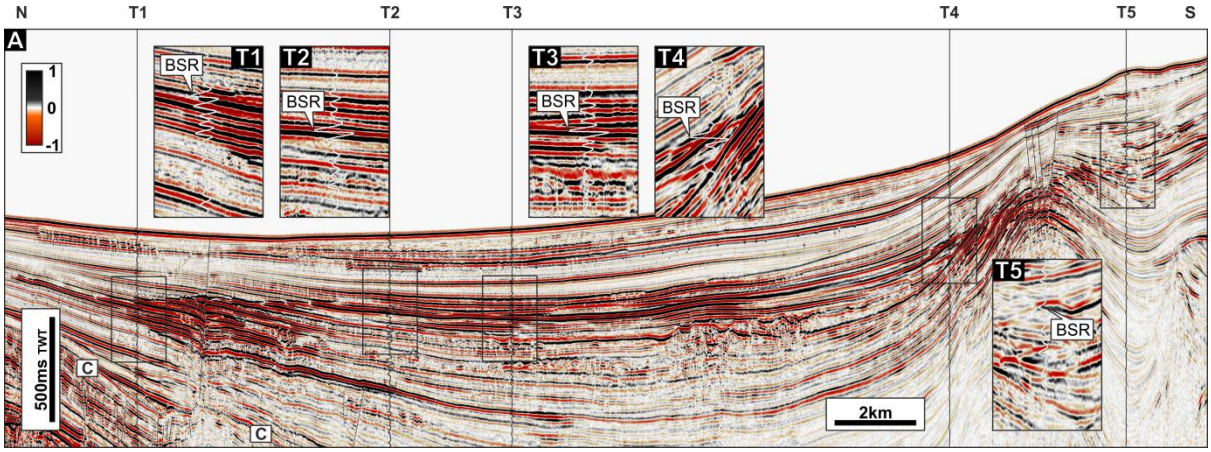

Figure 4.

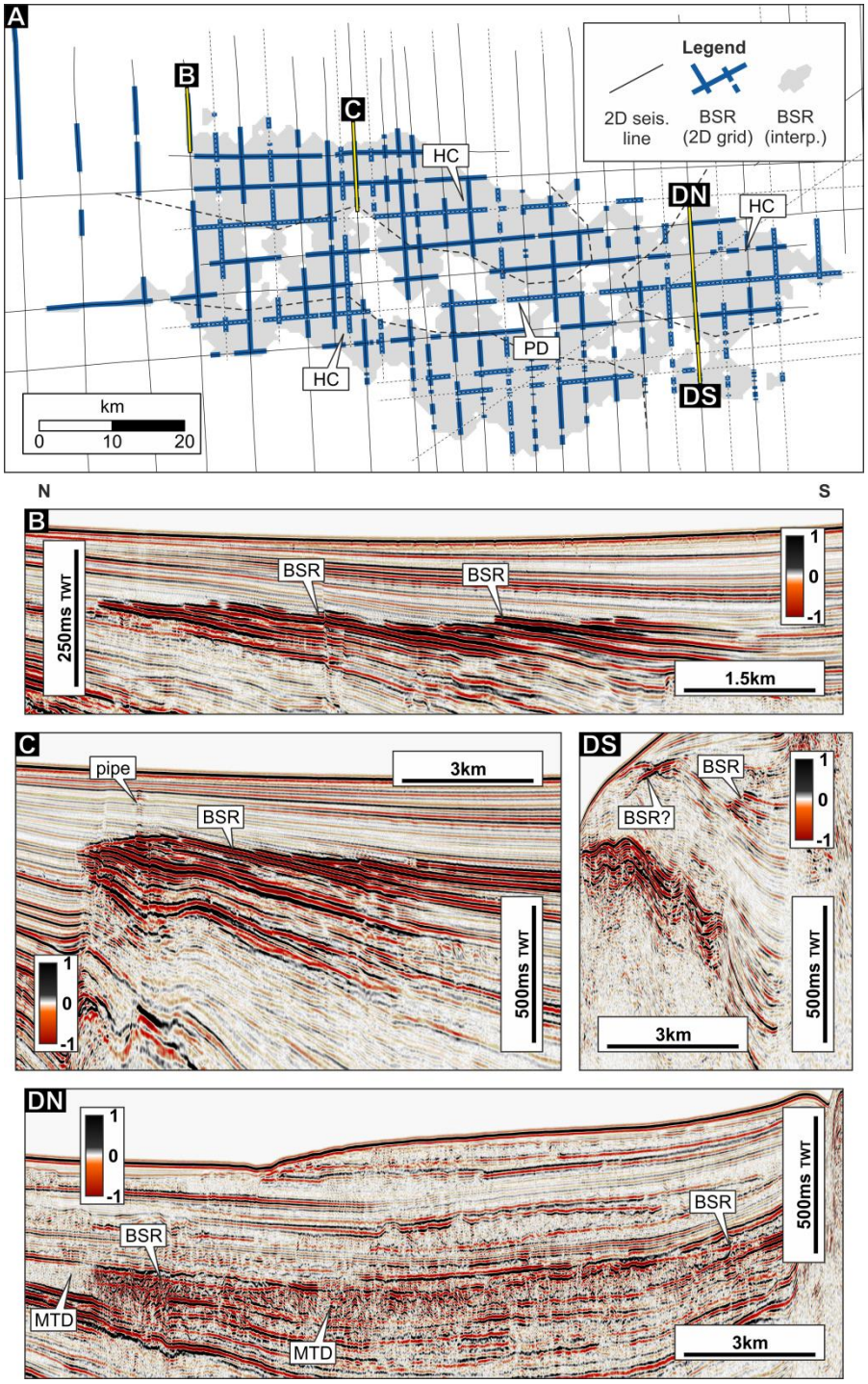
A
B
C
HC
DN
HC
PD
HC
DS
Legend
2D seis. line
BSR (2D grid)
BSR (interp.)
km
0
10
20
N
S
B
250ms TWT
BSR
BSR
1
0
-1
1.5km
C
pipe
BSR
3km
500ms TWT
DS
BSR
BSR?
3km
500ms TWT
DN
BSR
MTD
MTD
BSR
500ms TWT
3km

Figure 5.

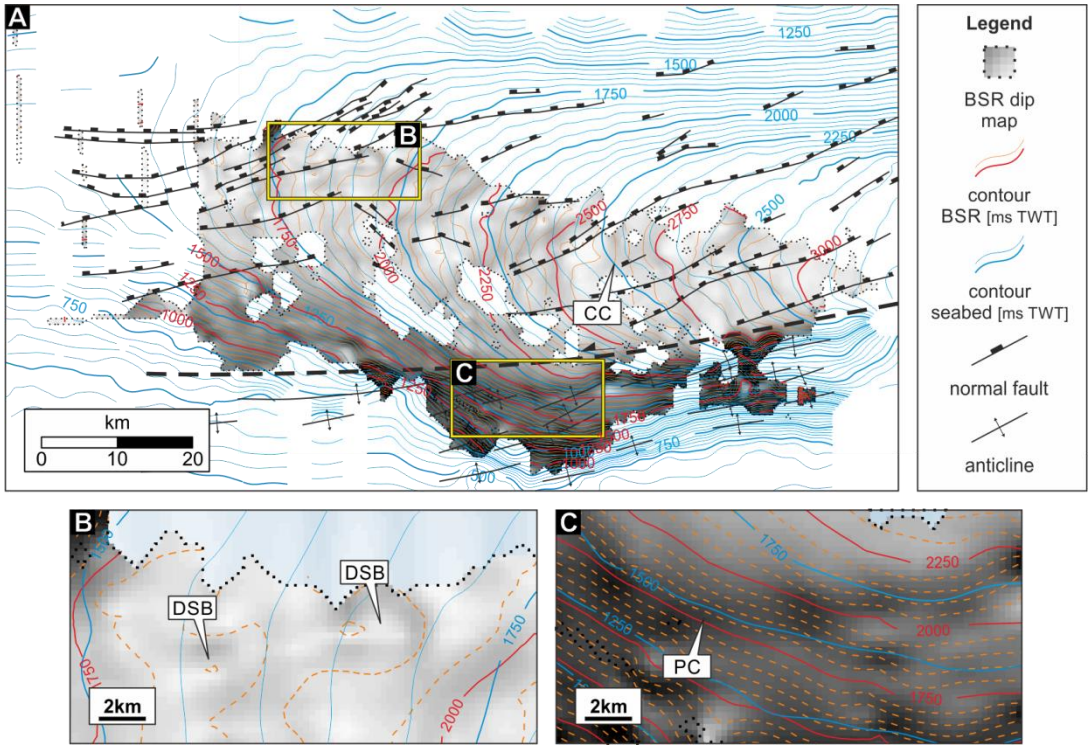
A
B
C
CC
km
0
10
20
Legend
BSR dip map
contour BSR [ms TWT]
contour seabed [ms TWT]
normal fault
anticline
DSB
DSB
2km
PC
2km

Figure 6.

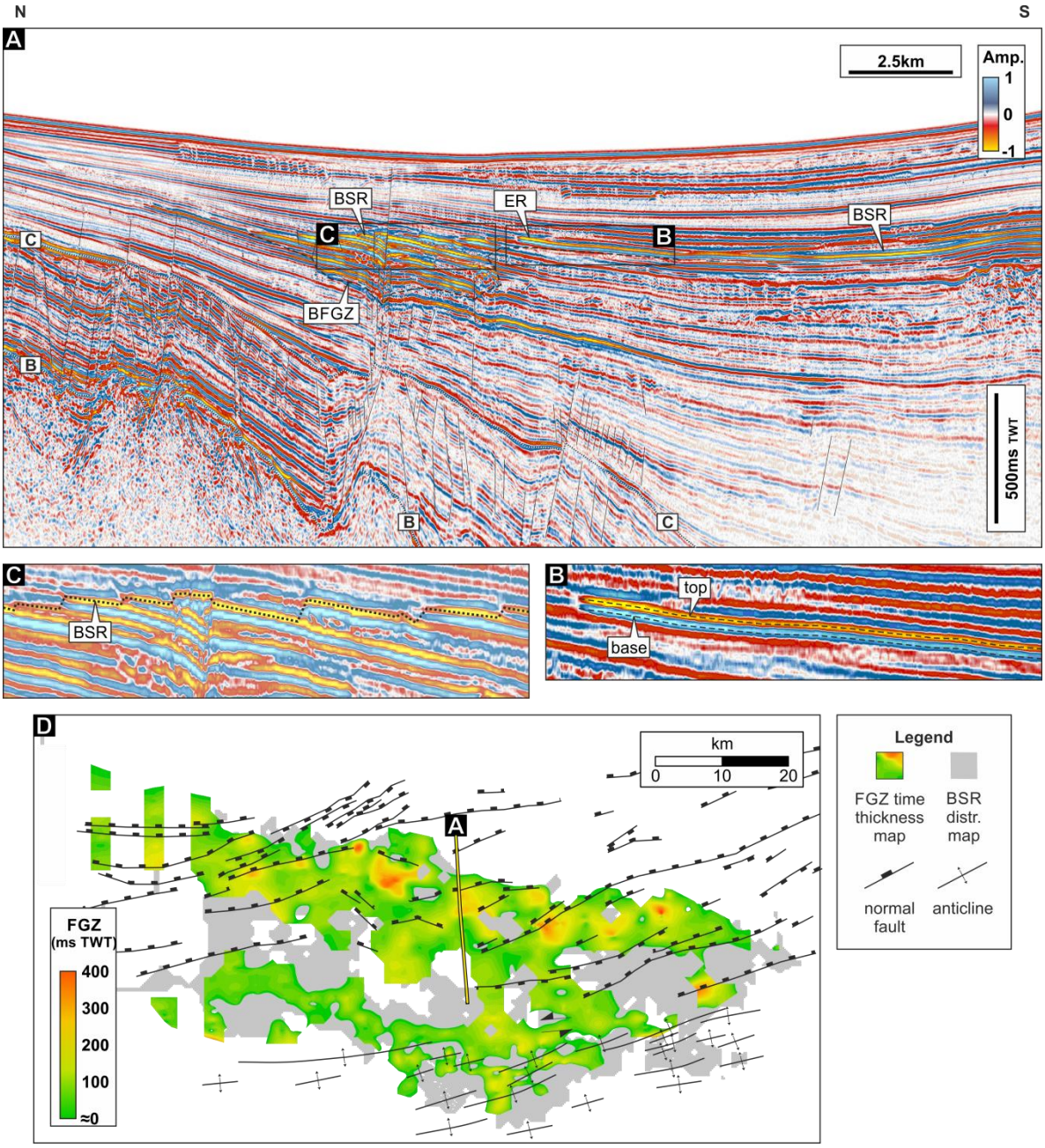
N
S
A
2.5km
Amp.
1
0
-1
BSR
ER
BSR
C
B
BFGZ
C
B
B
C
500ms TWT
C
BSR
B
top
base
D
km
0
10
20
A
FGZ
(ms TWT)
400
300
200
100
≈0
Legend
FGZ time thickness map
BSR distr. map
normal fault
anticline

Figure 7.

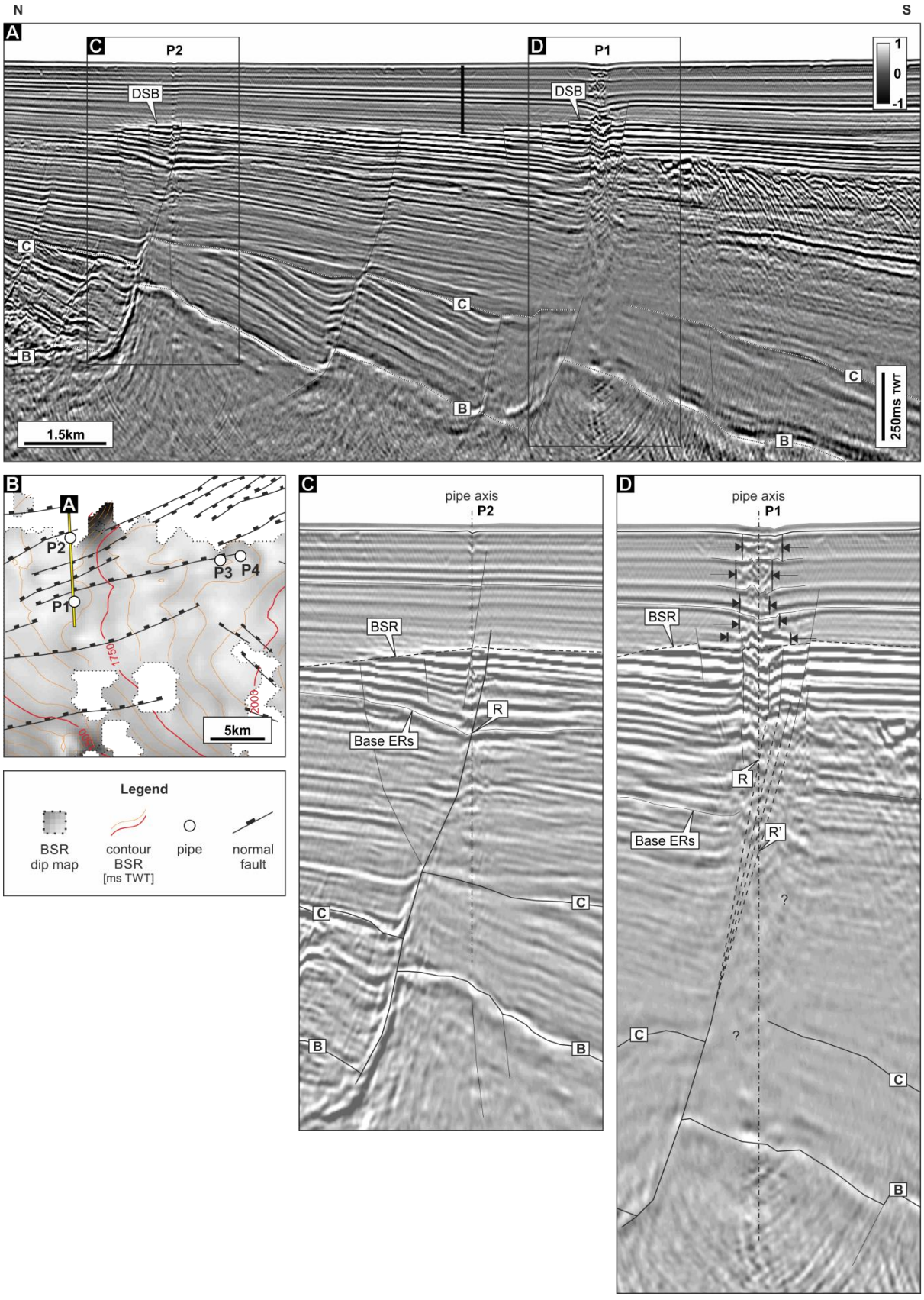
N
S
A
C
P2
D
P1
DSB
DSB
1
0
-1
C
C
B
B
C
B
1.5km
250ms TWT
B
A
P2
P1
P3
P4
1750
2000
2250
5km
Legend
BSR dip map
contour BSR [ms TWT]
pipe
normal fault
C
pipe axis
P2
BSR
R
Base ERs
C
B
B
D
pipe axis
P1
BSR
R
R'
Base ERs
?
?
C
C
B

Figure 8.

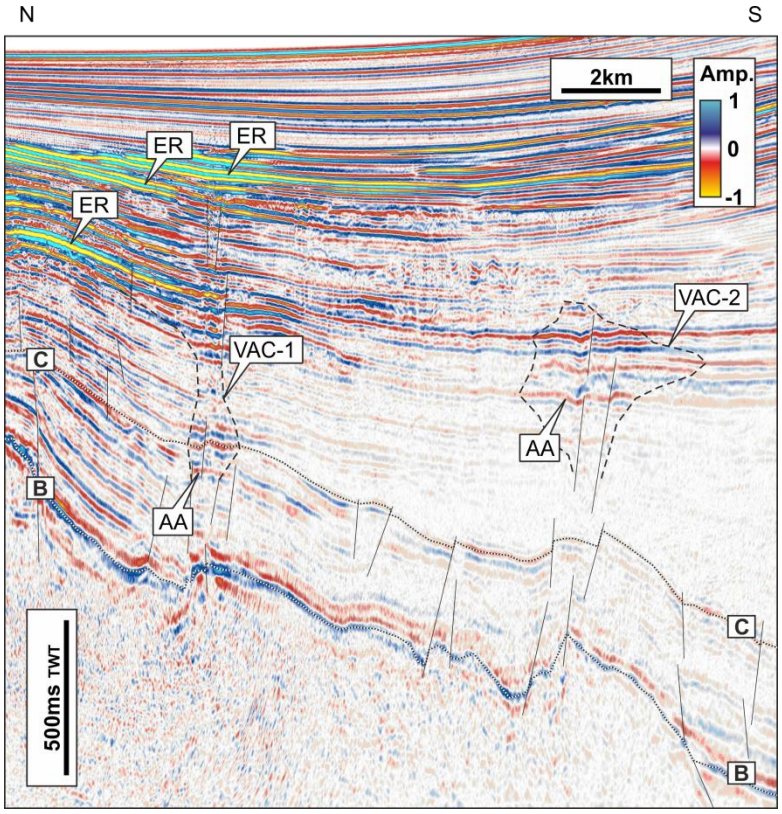

Figure 9.

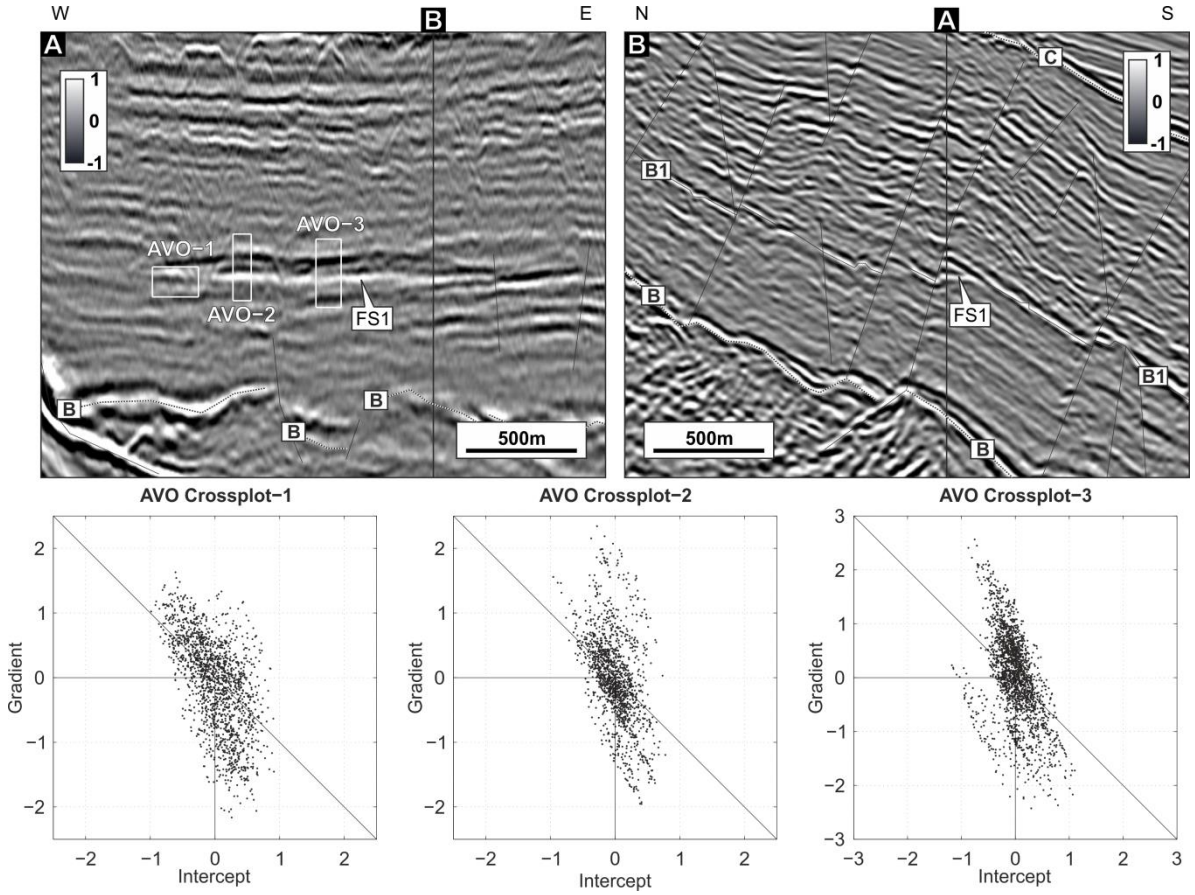
W
B
E
A
1
0
-1
AVO−1
AVO−2
AVO−3
FS1
B
B
B
500m
N
A
S
B
C
1
0
-1
B1
B
FS1
B1
500m
B
AVO Crossplot−1
AVO Crossplot−2
AVO Crossplot−3
Gradient
Intercept
Gradient
Intercept
Gradient
Intercept

Figure 10.

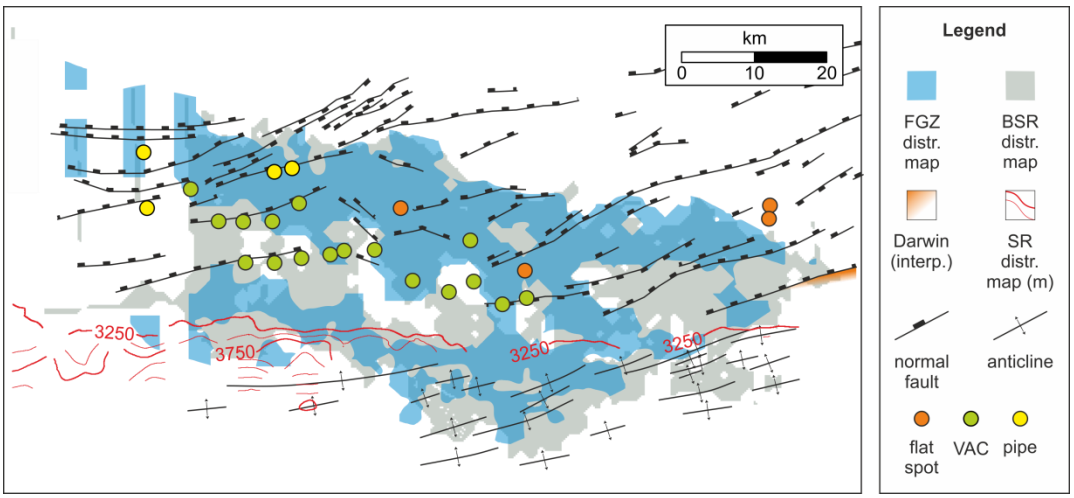
km
0
10
20
3250
3750
3250
3250
Legend
FGZ distr. map
BSR distr. map
Darwin (interp.)
SR distr. map (m)
normal fault
anticline
flat spot
VAC
pipe

Figure 11.